A gradient-damage theory for quasi brittle fracture

by

Sooraj Narayan

B.Tech(Hons.), Indian Institute of Technology - Madras (2017)

Submitted to the Department of Mechanical Engineering
in partial fulfillment of the requirements for the degree of

Master of Science

at the

Massachusetts Institute of Technology

June 2019

Signature redacted

Author . . . .
ᴜ
Department of Mechanical Engineering
May 16,2019

Signature redacted
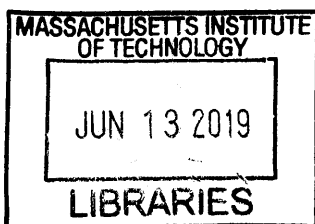
Certified by . . . .
Lallit Anand
Warren and Towneley Rohsenow Professor of Mechanical Engineering
Thesis Supervisor

Signature redacted

Accepted by . . . .
Nicolas Hadjiconstantinou
Chairman, Department Committee on Graduate Theses

A gradient-damage theory for quasi brittle fracture

by

Sooraj Narayan

Submitted to the Department of Mechanical Engineering
on May 16,2019, in partial fulfillment of the
requirements for the degree of
Master of Science

Abstract

Phase-field modeling of brittle fracture of linear elastic solids has been the subject of several studies in the past 25 years. An attractive feature of this approach to model fracture is its seamless ability to simulate the complicated fracture processes of nucleation, propagation, branching and merging of cracks in arbitrary geometries. While most existing models have focussed on fracture of "ideal brittle" materials, we consider fracture of "quasi-brittle" materials. The material is considered to be quasi-brittle in the sense that it does not lose its entire load-carrying capacity at the onset of damage. Instead there is a gradual degradation of the strength of the material, which is the result of microscale decohesion/damage micromechanisms.

In this thesis we discuss the formulation of our *gradient-damage theory* for quasi-brittle fracture using the *virtual-power method*. The macro- and microforce balances, obtained from the virtual power approach, together with a standard free-energy imbalance law under isothermal conditions, when supplemented with a set of thermodynamically-consistent constitutive equations will provide the governing equations for our theory. We have specialized our general theory to formulate a simple continuum model for fracture of concrete — a quasi-brittle material of vast importance. We have numerically implemented our theory in a finite element program, and simulated numerical examples which show the ability of the simulation capability to reproduce the macroscopic characteristics of the failure of concrete in several technically relevant geometries reported in the literature.

Thesis Supervisor: Lallit Anand
Title: Warren and Towneley Rohsenow Professor of Mechanical Engineering

Acknowledgments

First and foremost, I wish to thank Professor Lallit Anand, my thesis advisor for his invaluable guidance throughout my time at MIT. It has been a wonderful experience interacting and learning from him over the past couple of years and I hope to draw from my learnings in my future pursuits.

I would also like to thank other professors at MIT, whom I have had a chance to interact with through classes or otherwise. My peers - fellow graduate students in the mechanical engineering department have helped me academically as well as personally. I would like to specially thank Dr. Yunwei Mao, for helping me transition smoothly into graduate school and also for many insightful discussions.

I would like to dedicate this thesis to Appa and Amma (Dad and Mom), for motivating me throughout my academic journey. What I am today, I owe it completely to them. Thank you both for everything!

Contents

List of Figures

10

List of Tables

Chapter 1

Introduction

Phase-field modeling of brittle fracture of isotropic linear elastic solids has been the subject of several studies in the past 20 years. Major contributions to the field have been made by Francfort and Marigo (1998), Bourdin et al. (2000), Bourdin et al. (2008), Miehe and coworkers (cf., e.g., Miehe et al., 2010a,b, 2015), and Borden et al. (2012). In this approach to model fracture, one introduces a scalar order-parameter or "phase-field" variable $d \in [0, 1]$, which affects the energy storage and stiffness characteristics of the material. If $d = 0$ at a point then it is intact, while if $d = 1$ at some point, then it is fractured. Values of d between zero and one correspond to partially-fractured material. All fields remain continuous until the critical condition $d = 1$ is reached, and this gives rise to the nucleation of a "crack" with attendant small zones of high gradients of d and therefore stiffness. In the phase-field approach the evolution of d depends not only on d and other locally-defined variables, but also on the gradient of the phase-field parameter ∇d.

As reviewed by Ambati et al. (2015), phase-field modeling of brittle fracture overcomes the limitations of the classical Griffith sharp-crack theory. An attractive feature of the phase-field approach is its seamless ability to simulate the complicated fracture process of nucleation, propagation, branching and merging of cracks in arbitrary geometries — propagating cracks are tracked automatically by the evolution of the smooth phase-field d. This leads to a significant advantage over the discrete fracture models, whose numerical implementation requires special methods for

handling the discontinuities. In the phase-field approach the tedious task of tracking complicated crack surfaces is avoided, and this significantly simplifies its numerical implementation relative to the discrete crack formulations.

In contrast to fracture of "ideal brittle" materials, in this work we consider fracture of "quasi-brittle" materials. A material is considered to be quasi-brittle in the sense that it is a heterogeneous material with brittle constituents, which does not lose its entire load-carrying capacity at the onset of damage. Instead there is a gradual degradation of the strength of the material, which is the result of microscale decohesion/damage micromechanisms.

We focus in this thesis on modeling fracture of concrete, which is a quasi-brittle material of vast importance. In laboratory-sized concrete specimens,[1] the size of the fracture process zone ahead of the crack tip in these materials can become quite large — compared to the other structural dimensions — as the damage progresses on its path to total failure (Hillerborg et al., 1976; Bazant and Oh, 1983; Van Mier, 1991; Bazant and Planas, 1998; Elices et al., 2002; Bazant and Le, 2017).

To model such materials we make a constitutive assumption regarding their behavior — we consider some amount of local inelastic deformation that precedes the damage initiation and further drives the damage progression. The quasi-brittle nature of concrete is attributed to the bridging phenomena observed in these materials. The several micro-cracks that develop are bridged by the various aggregate particles present within. This bridging phenomena has been investigated over the past few decades and several researchers have reported on the bridging processes across length scales.

Van Mier (1991) and Schlangen and van Mier (1992) vacuum-impregnated single-edge notched plate tension specimens of concrete which were tested to a post-peak state, with a low-viscosity fluorescing epoxy. Using high-contrast imaging techniques they were able to reveal some fine-scale microstructural details in the macro-crack/damage-zone which they observed in their specimens. They observed that the damage-zone occurs primarily perpendicular to the direction of the maximum principal tensile stress, and that the faces of the crack-like features in the damage-zone were

---

[1]Less than 1m in some characteristic size such as the depth of a beam.

connected by ligaments which allow for some stress-transfer between the faces. To quote Van Mier (1991):

> "The macrocracks are highly discontinuous cracks with debonding near larger aggregates and intact material bridges between them. The load carrying capacity of a tensile specimen for average crack openings larger than 50μm can be explained from distributed crack interface grain bridging. The failure of the grain bridges is a process involving bending and frictional pull-out."

Such "crack face bridging" by aggregate particles was seen to occur for several different classes of concretes; one such observation is shown in the Fig. 1-1(a).

(a) (b)
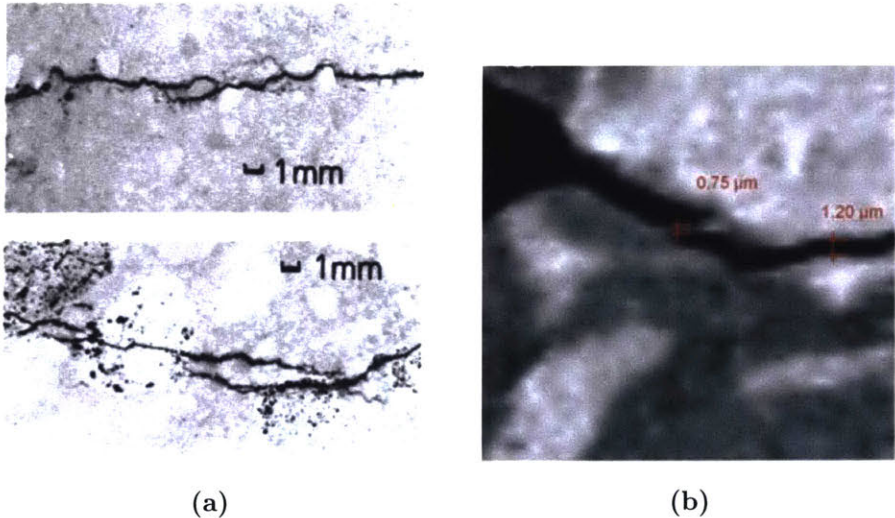
Figure 1-1: (a) Crack face bridging in concrete specimen observed by fluorescent epoxy impregnation. Taken from Schlangen and van Mier (1992). (b) Micro-CT scan of Portland cement showing evidences of the bridging phenomena. Taken from Trtik et al. (2007).

More recently, Trtik et al. (2007) conducted micro-tomography studies and observed similar bridging mechanisms at a much finer length scale in micro-tension specimens of Portland cement — one of the constituents of concrete — which is depicted in Fig. 1-1(b).

In the past two decades, great strides have been made in developing high performance polymer fiber-reinforced "engineered cementitious composites" which exhibit multiple-cracking and significant

inelastic behavior in uniaxial tension (Li, 2003). In these cementitous composites, crack face bridging is further enhanced by the polymer fibers. Fig. 1-2(a), taken from Wang and Li (2004), shows engineering stress-strain curves from direct tension tests on un-notched specimens on one such cementitious composite — a significant level of inelastic tensile strain, $\approx 4\%$, is clearly evident in this figure. Fig. 1-2(b) shows a representative photograph of the microcrack pattern observed on the surface of one of the specimens. Multiple microcracks with bridging fibers develop in the specimen perpendicular to the direction of the maximum principal tensile stress.

(a) (b)
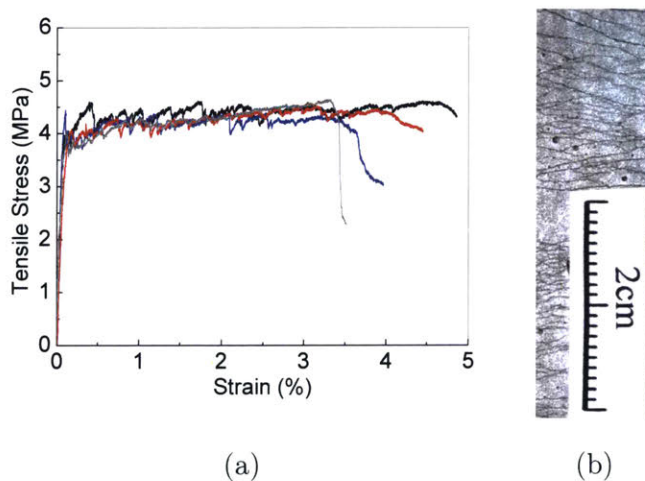
Figure 1-2: Fiber reinforced cementitious composite subjected to tension: (a) engineering stress-strain curves. (b) Microcracks with bridging fibers normal to loading direction. Taken from Wang and Li (2004).

We note that the process of inelastic deformation, damage, and fracture in concrete with distributed fibers *bears a certain similarity* to the "crazing" process which eventually leads to fracture in certain amorphous polymeric materials. A craze in a polymer is a planar crack-like defect that develops and expands normal to the maximum principal stress direction. Figure 1-3(a) shows a micrograph depicting several crack-like features developed during the crazing process in a loaded polymethyl-methacrylate (PMMA) specimen. Further, as can be seen from figure 1-3(b), that shows a microtomed polystyrene specimen, these crazes are usually bridged by micro-fibrils — hence the crack faces are not traction-free.
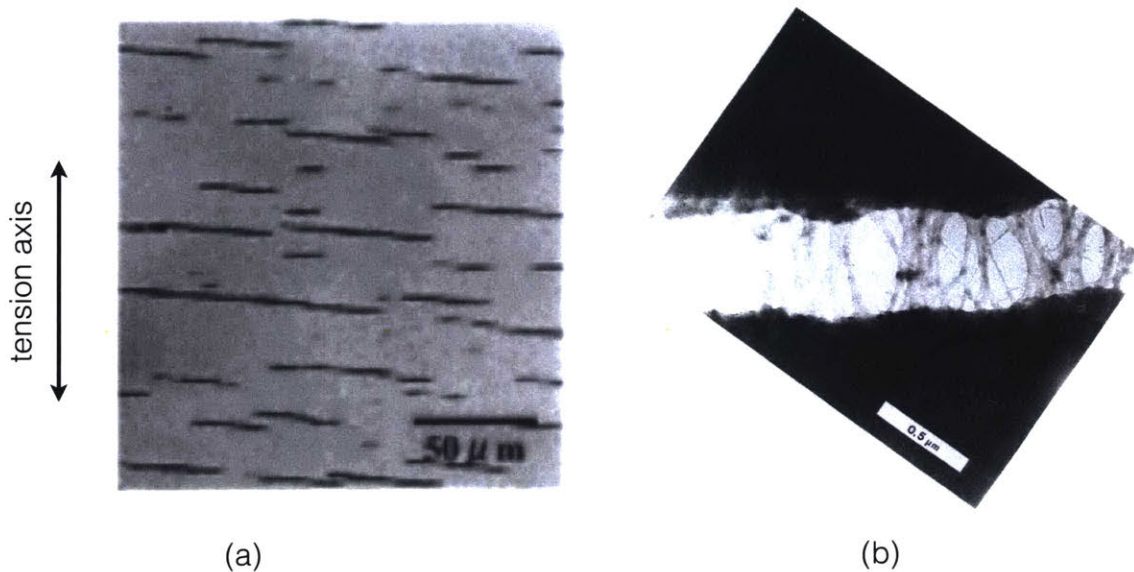
Figure 1-3: (a) Crazes developed perpendicular to the loading direction in a PMMA specimen. Taken from Ishiyama et al. (2001). (b)Microfibrils bridging across the crack faces of a craze in a polystyrene specimen. Taken from Argon and Hannoosh (1977).

It is based on this similarity between the macroscopic characteristics of inelastic deformation, damage, and failure in polymers and that of concrete, that we have borrowed the terminology of "crazing" from the polymer literature to describe the deformation and failure processes in concrete. In our view, whether it be in a polymer or in a concrete,

- *a craze is a planar crack-like defect that develops and expands inelastically normal to the maximum principal stress direction.*

We emphasize from the outset that while we borrow the terminology "crazing" from the polymer literature, we recognize that the crack-bridging micromechanisms leading to fracture in quasi-brittle materials like concrete (cf., e.g., Van Mier, 1991), are very different from those leading to craze formation, growth, and breakdown in polymers.

For the continuum level of interest here, the inelastic deformation due to crazing will be defined as an average over a microstructural representative volume element that results in an acceptably smooth process at the macroscopic level (prior to final fracture). We will introduce a simple craze initiation criterion based on the local maximum principal tensile stress reaching a critical value,

which we call the craze resistance. After crazing has initiated, our continuum model will allow for (a small amount of) craze-widening by dilational inelastic stretching which will be taken to occur in the direction of the local maximum principal stress. Finally, in order to model craze-breakdown and fracture, we develop a damage theory which depends not only on a damage variable d, but also its gradient ∇d, which represents a measure of the spatial inhomogeneity of the damage during the fracturing process. Hence there is a material length scale, ℓ, in the vicinity of a crack over which the damage variable d varies between zero and one, ℓ therefore represents a measure of the "width of the damage process zone". Another reason for introducing a gradient-damage theory is to "regularize" the strain-softening behavior during the fracture process as in Francfort and Marigo (1998), and to avoid mesh-dependency related issues during finite element simulations — as in the pioneering studies on fracture of quasi-brittle materials (cf., e.g., Pijaudier-Cabot and Bazant, 1987; Peerlings et al., 1996, 1998), and also in the more recent phase-field theories of fracture of brittle materials (cf., e.g., Miehe et al., 2010a,b, 2015; Borden et al., 2012). Numerically, a gradient theory can ensure that the simulation results are mesh-independent, provided the mesh size is small enough; that is, typical element size h_e less than $\approx 0.2\ell$.

There has been considerable recent activity in the research community to propose models for quasi-brittle fracture which use various non-local, gradient-damage, or phase-field-regularized cohesive zone models (cf., e.g., Lorentz, 2017; Wu, 2017; Wu et al., 2018, and the reference cited therein). The objectives of this thesis are similar to the objectives in these other recent efforts in the literature. However the details of our theory and its development are quite different. A major point of departure of our theory is that while most existing phase-field models of fracture have been formulated using a variational approach,[2] in this thesis we shall formulate our phase-field — or more precisely a *gradient-damage theory* — for fracture of quasi-brittle materials using an alternative approach. Specifically, we shall formulate the balances in our theory by following the pioneering *virtual-power method* of Germain (1973) and Gurtin (1996), and in a spirit similar to that of Fremond and Nedjar (1996) who first adopted the virtual-power method to formulate a gradient-damage theory. This approach leads to "macroforce" and "microforce" balances for the forces associated with the rate-like kinematical descriptors in the theory. These macro- and microforce balances, together with a

---

[2]Variational arguments, by their very nature, cannot adequately characterize the dissipation associated with inelasticity and fracture.

standard free-energy imbalance law under isothermal conditions, when supplemented with a set of thermodynamically-consistent constitutive equations will provide the governing equations for our theory. We have specialized our general theory to formulate a simple continuum model for fracture of concrete — a quasi-brittle material of vast importance. We present results from our numerical implementation that demonstrates it's capability to reproduce macroscopic failure response of concrete. Subsequently, we also show preliminary results of applicability of our model to materials other than concrete, when specialized suitably.

Chapter 2

Theoretical framework

This chapter concerns with the formulation of a thermodynamically-consisitent continuum mechanical damage model for a quasi-brittle fracture.

Our theory relates the following basic fields:[1]

---

[1] Notation: We use standard notation of modern continuum mechanics Gurtin et al. (2010). Specifically: ∇ and Div denote the gradient and divergence with respect to the material point $\mathbf{X}$ in the reference configuration; grad and div denote these operators with respect to the point $\mathbf{x} = \chi(\mathbf{X}, t)$ in the deformed body; a superposed dot denotes the material time-derivative. Throughout, we write $\mathbf{F}^{e-1} = (\mathbf{F}^e)^{-1}$, $\mathbf{F}^{e-\top} = (\mathbf{F}^e)^{-\top}$, etc. We write $\operatorname{tr}\mathbf{A}$, $\operatorname{sym}\mathbf{A}$, $\operatorname{skw}\mathbf{A}$, $\mathbf{A}_0$, and $\operatorname{sym}_0\mathbf{A}$ respectively, for the trace, symmetric, skew, deviatoric, and symmetric-deviatoric parts of a tensor $\mathbf{A}$. Also, the inner product of tensors $\mathbf{A}$ and $\mathbf{B}$ is denoted by $\mathbf{A}:\mathbf{B}$, and the magnitude of $\mathbf{A}$ by $|\mathbf{A}| = \sqrt{\mathbf{A}:\mathbf{A}}$.

$\mathbf{x} = \boldsymbol{\chi}(\mathbf{X}, t),$	motion;
$\mathbf{F} = \nabla\boldsymbol{\chi}, \quad J = \det \mathbf{F} > 0,$	deformation gradient;
$\mathbf{F} = \mathbf{F}^e\mathbf{F}^c,$	multiplicative decomposition of $\mathbf{F}$;
$\mathbf{F}^c, \quad J^c = \det \mathbf{F}^c > 1,$	inelastic craze distortion;
$\mathbf{F}^e, \quad J^e = \det \mathbf{F}^e > 0,$	elastic distortion;
$\mathbf{F}^e = \mathbf{R}^e\mathbf{U}^e,$	polar decomposition of $\mathbf{F}^e$;
$\mathbf{U}^e = \sum_{\alpha=1}^{3} \lambda_\alpha^e \mathbf{r}_\alpha^e \otimes \mathbf{r}_\alpha^e,$	spectral decomposition of $\mathbf{U}^e$;
$\mathbf{E}^e = \sum_{\alpha=1}^{3} (\ln \lambda_\alpha^e)\mathbf{r}_\alpha^e \otimes \mathbf{r}_\alpha^e,$	logarithmic elastic strain;
$\mathbf{M}^e,$	Mandel stress conjugate to logarithmic strain $\mathbf{E}^e$;
$\mathbf{T} = J^{e-1}\mathbf{R}^e\mathbf{M}^e\mathbf{R}^{e\mathsf{T}},$	Cauchy stress;
$\mathbf{T_R} = J\mathbf{T}\mathbf{F}^{-\mathsf{T}},$	Piola stress;
$\psi_{\mathrm{R}},$	free energy per unit reference volume;
$S^c > 0,$	craze resistance;
$\epsilon^c \geq 0,$	craze strain;
$\mathsf{d} \in [0, 1],$	damage variable;
$\nabla\mathsf{d},$	gradient of d;
$\ell > 0,$	length scale in the gradient damage theory.

We restrict our attention to isothermal conditions and assume that the material behavior may be modeled as isotropic.

2.1   Kinematics

Consider a macroscopically-homogeneous body B with the region of space it occupies in a fixed reference configuration, and denote by $\mathbf{X}$ an arbitrary material point of B. A motion of B is then a smooth one-to-one mapping $\mathbf{x} = \boldsymbol{\chi}(\mathbf{X}, t)$ with deformation gradient, velocity, and velocity gradient given by

$$\mathbf{F} = \nabla\boldsymbol{\chi}, \qquad \mathbf{v} = \dot{\boldsymbol{\chi}}, \qquad \mathbf{L} = \operatorname{grad} \mathbf{v} = \dot{\mathbf{F}}\mathbf{F}^{-1}. \tag{2.1}$$

We base our theory on the multiplicative decomposition of the deformation gradient,

$$\mathbf{F} = \mathbf{F}^e \mathbf{F}^c. \tag{2.2}$$

As is standard, we assume that

$$J \stackrel{\text{def}}{=} \det \mathbf{F} > 0, \tag{2.3}$$

and hence, using (2.2),

$$J = J^e J^c, \quad \text{and we assume that} \quad J^e \stackrel{\text{def}}{=} \det \mathbf{F}^e > 0 \quad \text{and} \quad J^c \stackrel{\text{def}}{=} \det \mathbf{F}^c > 0, \tag{2.4}$$

so that $\mathbf{F}^e$ and $\mathbf{F}^c$ are invertible. Here, suppressing the argument t:

(i) $\mathbf{F}^c(\mathbf{X})$ represents the local inelastic deformation in an infinitesimal neighborhood of material at $\mathbf{X}$ due to "crazing" which eventually culminates in a "quasi-brittle"-type failure.

(ii) $\mathbf{F}^e(\mathbf{X})$ represents the local deformation of material due to stretch and rotation of the microscopic structure.

We refer to $\mathbf{F}^c$ and $\mathbf{F}^e$ as the craze and elastic distortions, respectively.

The right polar decomposition of $\mathbf{F}^e$ is given by

$$\mathbf{F}^e = \mathbf{R}^e \mathbf{U}^e, \tag{2.5}$$

where $\mathbf{R}^e$ is a rotation, while $\mathbf{U}^e$ is a symmetric, positive-definite tensor with

$$\mathbf{U}^e = \sqrt{\mathbf{F}^{e\top} \mathbf{F}^e}. \tag{2.6}$$

As is standard, we define

$$\mathbf{C}^e = \mathbf{U}^{e2} = \mathbf{F}^{e\top} \mathbf{F}^e. \tag{2.7}$$

By (2.1)$_3$ and (2.2),

$$\mathbf{L} = \mathbf{L}^e + \mathbf{F}^e \mathbf{L}^c \mathbf{F}^{e-1}, \tag{2.8}$$

25

with

$$\mathbf{L}^e = \dot{\mathbf{F}}^e \mathbf{F}^{e-1}, \qquad \mathbf{L}^c = \dot{\mathbf{F}}^c \mathbf{F}^{c-1}. \tag{2.9}$$

As is standard, we define the elastic and craze stretching and spin tensors through

$$\mathbf{D}^e = \operatorname{sym} \mathbf{L}^e, \qquad \mathbf{W}^e = \operatorname{skw} \mathbf{L}^e, \qquad \mathbf{D}^c = \operatorname{sym} \mathbf{L}^c, \qquad \mathbf{W}^c = \operatorname{skw} \mathbf{L}^c, \tag{2.10}$$

so that $\mathbf{L}^e = \mathbf{D}^e + \mathbf{W}^e$ and $\mathbf{L}^c = \mathbf{D}^c + \mathbf{W}^c$.

We make the following additional kinematical assumption concerning craze flow:

(i) First, from the outset we constrain the theory by assuming that the craze flow is *irrotational,* in the sense that[2]

$$\mathbf{W}^c = \mathbf{0}. \tag{2.11}$$

Then, trivially, $\mathbf{L}^c \equiv \mathbf{D}^c$ and

$$\dot{\mathbf{F}}^c = \mathbf{D}^c \mathbf{F}^c. \tag{2.12}$$

On account of (2.11), the relation (2.8) reduces to

$$\mathbf{L} = \mathbf{L}^e + \mathbf{F}^e \mathbf{D}^c \mathbf{F}^{e-1}. \tag{2.13}$$

(ii) Second, we assume that $\mathbf{D}^c$ has the form (Gearing and Anand, 2004)

$$\mathbf{D}^c = \dot{\epsilon}^c \mathbf{N}^c \qquad \text{with} \qquad \mathbf{N}^c = \mathbf{m} \otimes \mathbf{m}, \tag{2.14}$$

where $\mathbf{m}$ is a unit vector (yet to be specified),

$$\dot{\epsilon}^c = |\mathbf{D}^c| \geq 0, \tag{2.15}$$

represents a *craze extension rate* in the direction $\mathbf{m}$. We call

$$\epsilon^c \overset{\text{def}}{=} \int_0^t \dot{\epsilon}^c(s)\, ds \tag{2.16}$$

---

[2]This assumption is adopted here solely on pragmatic grounds: when discussing finite deformations the theory without craze spin is far simpler than one with craze spin.

the *craze-strain.*

Thus, using (2.1), (2.2), and (2.14) we may write (2.13), for future use, as

$$(\nabla \dot{\boldsymbol{\chi}}) \mathbf{F}^{-1} = \dot{\mathbf{F}}^e \mathbf{F}^{e-1} + \dot{\epsilon}^c \, \mathbf{F}^e \, \mathbf{N}^c \, \mathbf{F}^{e-1}. \tag{2.17}$$

2.2 Damage variable

Next, in order to model the process of "craze-breakdown", we introduce a *damage variable* or *phase-field,*

$$\mathsf{d}(\mathbf{X}, t) \in [0, 1]. \tag{2.18}$$

If $\mathsf{d} = 0$ at a point then that point is intact, while if $\mathsf{d} = 1$ at some point, then that point is fractured. Values of d between zero and one correspond to partially-fractured material. We assume that d grows montonically so that

$$\dot{\mathsf{d}}(\mathbf{X}, t) \geq 0, \tag{2.19}$$

which is a constraint that represents an assumption that microstructural changes leading to damage are *irreversible.*

2.3 Method of virtual power. Balance of forces

We follow Gurtin (1996, 2002) and Gurtin et al. (2010) to derive macroscopic and microscopic force balances via the principle of virtual power. In developing our theory we take the "rate-like" kinematical descriptors to be $\dot{\boldsymbol{\chi}}$, $\dot{\mathbf{F}}^e$, $\dot{\epsilon}^c$, $\dot{\mathsf{d}}$, and also $\nabla \dot{\mathsf{d}}$. Also, in exploiting the principle of virtual power we note that the rates $(\dot{\boldsymbol{\chi}}, \dot{\mathbf{F}}^e, \dot{\epsilon}^c)$ are not independent — they are constrained by eq. (2.17).

We denote by P an arbitrary part of the reference body B, with $\mathbf{n}_{\mathrm{R}}$ the outward unit normal on the boundary ∂P of P. With each evolution of the body we associate macroscopic and microscopic force systems. The macroscopic system is defined by: (i) A traction $\mathbf{t}_{\mathrm{R}}(\mathbf{n}_{\mathrm{R}})$, for each unit vector $\mathbf{n}_{\mathrm{R}}$, that expends power over the velocity $\dot{\boldsymbol{\chi}}$, an external generalized body force $\mathbf{b}_{\mathrm{R}}$ that also expends power over $\dot{\boldsymbol{\chi}}$. That is,

$$\mathbf{b}_{\mathrm{R}} = \mathbf{b}_{0\mathrm{R}} - \rho_{\mathrm{R}} \ddot{\boldsymbol{\chi}}, \tag{2.20}$$

27

where $\mathbf{b}_{0R}$ represents the conventional body force per unit volume of the reference body, and $(-\rho_R\ddot{\boldsymbol{\chi}})$ represents the inertial body force; ρ_R is the mass density of the referential body. (ii) An elastic stress $\mathbf{S}^e$ that expends power over the elastic distortion rate $\dot{\tilde{\mathbf{F}}}^e$.

The microscopic system is defined by: (a) A positive-valued scalar microscopic stress π that expends power over the craze strain rate $\dot{\epsilon}^c$. (b) A scalar microscopic stress ϖ that expends power over the rate, $\dot{\mathbf{d}}$, of the damage variable, $\mathbf{d}$. (c) A vector microscopic stress $\boldsymbol{\xi}$ that expends power over the gradient $\nabla\dot{\mathbf{d}}$. And (d) A scalar microscopic traction $\xi(\mathbf{n}_R)$ that expends power over $\dot{\mathbf{d}}$ on the boundary of the part.

We characterize the force systems through the manner in which these forces expend power; that is, given any part P, through the specification of $\mathcal{W}_{ext}(P)$, the power expended on P by material *external* to P, and $\mathcal{W}_{int}(P)$, a concomitant expenditure of power *within* P. Specifically,

$$
\begin{aligned}
\mathcal{W}_{ext}(P) &= \int_{\partial P} \mathbf{t}_R(\mathbf{n}_R) \cdot \dot{\boldsymbol{\chi}}\, da_R + \int_P \mathbf{b}_R \cdot \dot{\boldsymbol{\chi}}\, dv_R + \int_{\partial P} \xi(\mathbf{n}_R)\dot{\mathbf{d}}\, da_R, \\
\mathcal{W}_{int}(P) &= \int_P \left(\mathbf{S}^e : \dot{\mathbf{F}}^e + \pi\dot{\epsilon}^c + \varpi\dot{\mathbf{d}} + \boldsymbol{\xi}\cdot\nabla\dot{\mathbf{d}} \right) dv_R.
\end{aligned}
\tag{2.21}
$$

Assume that, at some arbitrarily chosen but *fixed time*, the fields $\boldsymbol{\chi}$, $\mathbf{F}^e$ (and hence $\mathbf{F}$ and $\mathbf{F}^c$), and $\mathbf{N}^c$ are known, and consider the fields $\dot{\boldsymbol{\chi}}$, $\dot{\mathbf{F}}^e$, and $\dot{\epsilon}^c$ as virtual velocities to be specified independently in a manner consistent with (2.17); that is, denoting the virtual fields by $\tilde{\boldsymbol{\chi}}$, $\tilde{\mathbf{F}}^e$, and $\tilde{\epsilon}^c$ to differentiate them from fields associated with the actual evolution of the body, we require that

$$
(\nabla\tilde{\boldsymbol{\chi}})\mathbf{F}^{-1} = \tilde{\mathbf{F}}^e\mathbf{F}^{e-1} + \tilde{\epsilon}^c\mathbf{F}^e\,\mathbf{N}^c\,\mathbf{F}^{e-1}.
\tag{2.22}
$$

Further, also considering $\dot{\mathbf{d}}$ to be a virtual velocity, and denoting its virtual counterpart by $\tilde{\mathbf{d}}$, we define a generalized virtual velocity to be a list

$$
\mathcal{V} = (\tilde{\boldsymbol{\chi}}, \tilde{\mathbf{F}}^e, \tilde{\epsilon}^c, \tilde{\mathbf{d}}),
$$

consistent with (2.22).

28

We refer to a macroscopic virtual field $\mathcal{V}$ as *rigid* if it satisfies

$$(\nabla\tilde{\chi}) = \tilde{\mathbf{F}} = \boldsymbol{\Omega}\mathbf{F}, \tag{2.23}$$

with $\boldsymbol{\Omega}$ a spatially constant skew tensor, together with

$$\tilde{\mathbf{F}}^e = \boldsymbol{\Omega}\mathbf{F}^e, \quad \tilde{\epsilon}^c = 0, \quad \tilde{\mathsf{d}} = 0. \tag{2.24}$$

Writing

$$\mathcal{W}_{\text{ext}}(\mathrm{P}, \mathcal{V}) = \int_{\partial\mathrm{P}} \mathbf{t}_{\mathrm{R}}(\mathbf{n}_{\mathrm{R}}) \cdot \tilde{\chi}\, da_{\mathrm{R}} + \int_{\mathrm{P}} \mathbf{b}_{\mathrm{R}} \cdot \tilde{\chi}\, dv_{\mathrm{R}} + \int_{\partial\mathrm{P}} \xi(\mathbf{n}_{\mathrm{R}})\, \tilde{\mathsf{d}}\, da_{\mathrm{R}},$$

$$\mathcal{W}_{\text{int}}(\mathrm{P}, \mathcal{V}) = \int_{\mathrm{P}} \left(\mathbf{S}^e : \tilde{\mathbf{F}}^e + \pi\tilde{\epsilon}^c + \varpi\tilde{\mathsf{d}} + \boldsymbol{\xi} \cdot \nabla\tilde{\mathsf{d}} \right) dv_{\mathrm{R}}, \tag{2.25}$$

respectively, for the external and internal expenditures of virtual power, the *principle of virtual power* consists of two basic requirements:

(V1) Given any part P,

$$\mathcal{W}_{\text{ext}}(\mathrm{P}, \mathcal{V}) = \mathcal{W}_{\text{int}}(\mathrm{P}, \mathcal{V}) \quad \text{for all generalized virtual velocities } \mathcal{V}. \tag{2.26}$$

(V2) Given any part P and a *rigid* virtual velocity $\mathcal{V}$,

$$\mathcal{W}_{\text{int}}(\mathrm{P}, \mathcal{V}) = 0 \tag{2.27}$$

2.4 Consequences of the principle of virtual power

The virtual-power principle has the following consequences:

(a) The stress

$$\mathbf{T}_{\mathrm{R}} \stackrel{\text{def}}{=} \mathbf{S}^e \mathbf{F}^{c-\top}, \tag{2.28}$$

is consistent with a macroscopic force balance and a macroscopic traction condition,

$$\text{Div } \mathbf{T}_{\mathrm{R}} + \mathbf{b}_{0\mathrm{R}} = \rho_{\mathrm{R}}\ddot{\chi} \quad \text{and} \quad \mathbf{t}_{\mathrm{R}}(\mathbf{n}_{\mathrm{R}}) = \mathbf{T}_{\mathrm{R}}\mathbf{n}_{\mathrm{R}}, \tag{2.29}$$

29

and $\mathbf{T_R F^\top}$ is symmetric,

$$\mathbf{T_R F^\top} = \mathbf{F T_R^\top}. \tag{2.30}$$

In view of (2.29) and (2.30) the stress $\mathbf{T_R}$ represents the classical Piola stress, with (2.29) and (2.30) representing the local macroscopic force and moment balances in the reference body.

As is standard, the symmetric Cauchy stress $\mathbf{T}$ in the deformed body is related to the Piola stress by

$$\mathbf{T} = J^{-1} \mathbf{T_R F^\top}. \tag{2.31}$$

It is convenient to introduce two new stress measures:

- The elastic second Piola stress,

$$\mathbf{T}^e \stackrel{\text{def}}{=} J^e \mathbf{F}^{e-1} \mathbf{T F}^{e-\top}, \tag{2.32}$$

 which is *symmetric* on account of the symmetry of the Cauchy stress $\mathbf{T}$.

- The Mandel stress,

$$\mathbf{M}^e \stackrel{\text{def}}{=} \mathbf{C}^e \mathbf{T}^e = J^e \mathbf{F}^{e\top} \mathbf{T F}^{e-\top}. \tag{2.33}$$

 which in general is *not symmetric*.

Using (2.28) and (2.31) we find that

$$\mathbf{S}^e = J \mathbf{T F}^{e-\top}. \tag{2.34}$$

Thus, using the definitions (2.32) and (2.33) we find that

$$\mathbf{F}^{e-1} \mathbf{S}^e = J^c \mathbf{T}^e \quad \text{and} \quad \mathbf{F}^{e\top} \mathbf{S}^e = J^c \mathbf{M}^e. \tag{2.35}$$

(b) A microscopic force balance,

$$\sigma = \pi, \tag{2.36}$$

where σ is a *resolved tensile stress* defined by the relation

$$\sigma \overset{\text{def}}{=} J^c \mathbf{M}^e : \mathbf{N}^c .$$

(2.37)

(c) The microstresses $\boldsymbol{\xi}$ and ϖ are consistent with the microforce balance and microtraction condition,

$$\text{Div}\,\boldsymbol{\xi} - \varpi = 0, \qquad \text{and} \qquad \xi(\mathbf{n}_\text{R}) = \boldsymbol{\xi} \cdot \mathbf{n}_\text{R}.$$

(2.38)

These macro- and microforce balances, when supplemented with a set of thermodynamically consistent constitutive equations, provide the governing mechanical equations for the theory.

Finally, using the traction conditions $(2.29)_2$, and $(2.38)_2$ the actual external expenditure of power (2.21) may be written as

$$\mathcal{W}_\text{ext}(\text{P}) = \int_{\partial \text{P}} (\mathbf{T}_\text{R} \mathbf{n}_\text{R}) \cdot \dot{\boldsymbol{\chi}}\, da_\text{R} + \int_\text{P} \mathbf{b}_\text{R} \cdot \dot{\boldsymbol{\chi}}\, dv_\text{R} + \int_{\partial \text{P}} (\boldsymbol{\xi} \cdot \mathbf{n}_\text{R})\dot{\mathsf{d}}\, da_\text{R}.$$

(2.39)

Also, using $(2.35)_1$ and (2.7), the stress power $\mathbf{S}^e : \dot{\mathbf{F}}^e$ may be alternatively written as

$$\mathbf{S}^e : \dot{\mathbf{F}}^e = \frac{1}{2} J^c \mathbf{T}^e : \dot{\mathbf{C}}^e.$$

(2.40)

Thus, the corresponding actual internal expenditure of power $(2.21)_1$ may be written as

$$\mathcal{W}_\text{int}(\text{P}) = \int_\text{P} \left(\frac{1}{2} J^c \mathbf{T}^e : \dot{\mathbf{C}}^e + \pi \dot{\epsilon}^c + \varpi \dot{\mathsf{d}} + \boldsymbol{\xi} \cdot \nabla \dot{\mathsf{d}} \right) dv_\text{R}.$$

(2.41)

2.5   Free-energy imbalance

Under isothermal conditions the two laws of thermodynamics reduce to the statement that *the temporal increase in free energy of any part P is less than or equal to the power expended on P.* Precisely, letting ψ_R denote the free energy per unit reference volume, this requirement takes the form of a *free-energy imbalance* (Gurtin et al., 2010)

$$\overline{\int_\text{P} \psi_\text{R}\, dv_\text{R}} \leq \mathcal{W}_\text{ext}(\text{P}).$$

(2.42)

31

Since $\mathcal{W}_{\text{ext}}(\text{P}) = \mathcal{W}_{\text{int}}(\text{P})$, using (2.41) we obtain

$$\int_{\text{P}} \left(\dot{\psi}_{\text{R}} - \left(\frac{1}{2} J^c \mathbf{T}^e : \dot{\mathbf{C}}^e + \pi \dot{\epsilon}^c + \varpi \dot{\mathsf{d}} + \boldsymbol{\xi} \cdot \nabla \dot{\mathsf{d}} \right) \right) dv_{\text{R}} \leq 0, \tag{2.43}$$

which upon using the fact that (2.43) must hold for all parts P, yields the following local *free-energy imbalance under isothermal conditions,*

$$\dot{\psi}_{\text{R}} - \frac{1}{2} J^c \mathbf{T}^e : \dot{\mathbf{C}}^e - \pi \dot{\epsilon}^c - \varpi \dot{\mathsf{d}} - \boldsymbol{\xi} \cdot \nabla \dot{\mathsf{d}} \leq 0 \,. \tag{2.44}$$

Remark. For brevity we have not discussed invariance properties of the various fields appearing in our theory. Here, we simply note that all quantities in the free energy imbalance (2.44) are invariant under a change in frame. $\square$

2.6 Constitutive theory

By (2.15) the craze inelastic strain satisfies

$$\epsilon^c(\mathbf{X}, 0) = 0, \qquad \dot{\epsilon}^c(\mathbf{X}, t) \geq 0, \tag{2.45}$$

and hence ϵ^c increases with time in any "inelastic process". We view ϵ^c as a measure of the past history of inelastic strain in the material. Recall that we have also introduced an additional damage variable d. Here we consider a theory which allows for an energetic and dissipative effects associated with temporal changes in d, and also an energetic effect due to the gradient $\nabla \mathsf{d}$. We consider the gradient $\nabla \mathsf{d}$ as a measure of the inhomogeneity of the microscale damage.

Guided by the free-energy imbalance (2.44), we consider $\mathbf{C}^e$, ϵ^c, and d as *independent variables,* and we consider the following set of constitutive equations for the free energy ψ_{R}, the stress $\mathbf{T}^e$, and $\boldsymbol{\xi}$ the vector microforce:

$$\psi_{\text{R}} = \hat{\psi}_{\text{R}}(\boldsymbol{\Lambda}), \qquad \mathbf{T}^e = \hat{\mathbf{T}}^e(\boldsymbol{\Lambda}), \qquad \boldsymbol{\xi} = \hat{\boldsymbol{\xi}}(\boldsymbol{\Lambda}), \tag{2.46}$$

32

where $\mathbf{\Lambda}$ denotes the list

$$\mathbf{\Lambda} = (\mathbf{C}^e, \epsilon^c, \mathsf{d}, \nabla \mathsf{d}). \tag{2.47}$$

Substituting the constitutive equation $(2.46)_1$ into the free-energy imbalance (2.44), we find that it may be written as,

$$\left(\frac{\partial \hat{\psi}_{\mathrm{R}}(\mathbf{\Lambda})}{\partial \mathbf{C}^e} - \frac{1}{2} J^c \hat{\mathbf{T}}^e(\mathbf{\Lambda}) \right) : \dot{\mathbf{C}}^e - \left(\pi - \frac{\partial \hat{\psi}_{\mathrm{R}}(\mathbf{\Lambda})}{\partial \epsilon^c} \right) \dot{\epsilon}^c - \left(\varpi - \frac{\partial \hat{\psi}_{\mathrm{R}}(\mathbf{\Lambda})}{\partial \mathsf{d}} \right) \dot{\mathsf{d}} - \left(\boldsymbol{\xi} - \frac{\partial \hat{\psi}_{\mathrm{R}}(\mathbf{\Lambda})}{\partial \nabla \mathsf{d}} \right) \cdot \nabla \dot{\mathsf{d}} \le 0. \tag{2.48}$$

We assume that the free energy function $\hat{\psi}_{\mathrm{R}}(\mathbf{\Lambda})$ delivers the stress $\mathbf{T}^e$ and the vector microstress $\boldsymbol{\xi}$ through the state relations

$$\mathbf{T}^e = 2 \, J^{c-1} \frac{\partial \hat{\psi}_{\mathrm{R}}(\mathbf{\Lambda})}{\partial \mathbf{C}^e}, \qquad \boldsymbol{\xi} = \frac{\partial \hat{\psi}_{\mathrm{R}}(\mathbf{\Lambda})}{\partial \nabla \mathsf{d}}. \tag{2.49}$$

Further, upon introducing energetic microstresses π_{en} and ϖ_{en} through the relations,

$$\pi_{\mathrm{en}} = \frac{\partial \hat{\psi}_{\mathrm{R}}(\mathbf{\Lambda})}{\partial \epsilon^c} \qquad \text{and} \qquad \varpi_{\mathrm{en}} = \frac{\partial \hat{\psi}_{\mathrm{R}}(\mathbf{\Lambda})}{\partial \mathsf{d}}, \tag{2.50}$$

and a dissipative microstresses π_{dis} and ϖ_{dis} through the relations

$$\pi_{\mathrm{dis}} = \pi - \pi_{\mathrm{en}} \qquad \text{and} \qquad \varpi_{\mathrm{dis}} = \varpi - \varpi_{\mathrm{en}}, \tag{2.51}$$

we are left with the following reduced dissipation inequality

$$\mathcal{D} = \pi_{\mathrm{dis}} \dot{\epsilon}^c + \varpi_{\mathrm{dis}} \dot{\mathsf{d}} \ge 0. \tag{2.52}$$

We assume that the terms in (2.52) individually satisfy the dissipation inequalities

$$\pi_{\mathrm{dis}} \dot{\epsilon}^c \ge 0, \quad \varpi_{\mathrm{dis}} \dot{\mathsf{d}} \ge 0. \tag{2.53}$$

In the following sections we introduce special constitutive equations which should be useful in applications.

2.7 Free energy

Henceforth we restrict our attention to isotropic materials for which the response function $\hat{\psi}_R(\boldsymbol{\Lambda})$ is taken to depend on $\mathbf{C}^e$ only through its principal invariants

$$\mathcal{I}_{\mathbf{C}^e} = (I_1(\mathbf{C}^e), I_2(\mathbf{C}^e), I_3(\mathbf{C}^e)), \tag{2.54}$$

and that the dependence on $\nabla \mathsf{d}$ is through its magnitude $|\nabla \mathsf{d}|$, so that the free energy function $(2.46)_1$ becomes[3]

$$\psi_R = \hat{\psi}_R(\mathcal{I}_{\mathbf{C}^e}, \epsilon^c, \mathsf{d}, |\nabla \mathsf{d}|). \tag{2.55}$$

Thus, from (2.49), it follows that the constitutive equation for $\mathbf{T}^e$ is,

$$\mathbf{T}^e = 2\, J^{c-1}\, \frac{\partial\, \hat{\psi}_R(\mathcal{I}_{\mathbf{C}^e}, \epsilon^c, \mathsf{d}, |\nabla \mathsf{d}|)}{\partial \mathbf{C}^e}, \tag{2.56}$$

and

$$\boldsymbol{\xi} = \frac{\partial \hat{\psi}_R(\mathcal{I}_{\mathbf{C}^e}, \epsilon^c, \mathsf{d}, |\nabla \mathsf{d}|)}{\partial \nabla \mathsf{d}}, \tag{2.57}$$

and that the constitutive equation for $\mathbf{T}^e$ is an *isotropic function* of $\mathbf{C}^e$. Then since the Mandel stress is defined by (cf. (2.33))

$$\mathbf{M}^e = \mathbf{C}^e \mathbf{T}^e, \tag{2.58}$$

we find that $\mathbf{T}^e$ and $\mathbf{C}^e$ commute,

$$\mathbf{C}^e \mathbf{T}^e = \mathbf{T}^e \mathbf{C}^e, \tag{2.59}$$

and hence that *the Mandel stress is symmetric*.

Now, the spectral representation of $\mathbf{C}^e$ is $\mathbf{C}^e = \sum_{i=1}^{3}(\lambda_i^e)^2 \mathbf{r}_i^e \otimes \mathbf{r}_i^e$, where $(\mathbf{r}_1^e, \mathbf{r}_2^e, \mathbf{r}_3^e)$ are the orthonormal eigenvectors of $\mathbf{C}^e$ and $\mathbf{U}^e$, and $(\lambda_1^e, \lambda_2^e, \lambda_3^e)$ are the positive eigenvalues of $\mathbf{U}^e$. Instead of using the invariants $\mathcal{I}_{\mathbf{C}^e}$, the free energy ψ_R may be alternatively expressed in terms of the principal stretches as,

$$\psi_R = \breve{\psi}_R(\lambda_1^e, \lambda_2^e, \lambda_3^e, \epsilon^c, \mathsf{d}, |\nabla \mathsf{d}|). \tag{2.60}$$

---

[3]We neglect any dependence on the joint invariants of $\mathbf{C}^e$ and $\nabla \mathsf{d}$.

Let

$$\mathbf{E}^e \stackrel{\text{def}}{=} \ln \mathbf{U}^e = \sum_{i=1}^{3} E_i^e \mathbf{r}_i^e \otimes \mathbf{r}_i^e \qquad \text{with} \qquad E_i^e \stackrel{\text{def}}{=} \ln \lambda_i^e, \tag{2.61}$$

denote the logarithmic elastic strain with principal values E_i^e, and consider a free energy function of the form

$$\breve{\psi}_{\mathrm{R}}(\lambda_1^e, \lambda_2^e, \lambda_3^e, \epsilon^c, \mathsf{d}, |\nabla \mathsf{d}|) = \breve{\psi}_{\mathrm{R}}(E_1^e, E_2^e, E_3^e, \epsilon^c, \mathsf{d}, |\nabla \mathsf{d}|). \tag{2.62}$$

Then, the Mandel stress is given by

$$\mathbf{M}^e = J^{c-1} \sum_{i=1}^{3} \frac{\partial \breve{\psi}_{\mathrm{R}}(E_1^e, E_2^e, E_3^e, \epsilon^c, \mathsf{d}, |\nabla \mathsf{d}|)}{\partial E_i^e} \mathbf{r}_i^e \otimes \mathbf{r}_i^e. \tag{2.63}$$

With the logarithmic strain defined by (2.61), and bearing in mind (2.62) and (2.63), we henceforth consider a free energy of the form

$$\psi_{\mathrm{R}} = \tilde{\psi}_{\mathrm{R}}(\mathcal{I}_{\mathbf{E}^e}, \epsilon^c, \mathsf{d}, |\nabla \mathsf{d}|), \tag{2.64}$$

with $\mathcal{I}_{\mathbf{E}^e}$ a list of principal invariants of $\mathbf{E}^e$, or equivalently a list of principal values of $\mathbf{E}^e$. The Mandel stress is then given by

$$\mathbf{M}^e = J^{c-1} \frac{\partial \tilde{\psi}_{\mathrm{R}}(\mathcal{I}_{\mathbf{E}^e}, \epsilon^c, \mathsf{d}, |\nabla \mathsf{d}|)}{\partial \mathbf{E}^e}, \tag{2.65}$$

and the corresponding Cauchy stress is

$$\mathbf{T} = J^{e-1} \mathbf{R}^e \mathbf{M}^e \mathbf{R}^{e\top}. \tag{2.66}$$

As a further specialization we consider a free energy of the form,

$$\tilde{\psi}_{\mathrm{R}}(\mathcal{I}_{\mathbf{E}^e}, \epsilon^c, \mathsf{d}, |\nabla \mathsf{d}|) = g(\mathsf{d}) J^c \left[\tilde{\psi}^e(\mathcal{I}_{\mathbf{E}^e}) + \tilde{\psi}^c(\epsilon^c) \right] + A |\nabla \mathsf{d}|^2. \tag{2.67}$$

In (2.67) the term $\left[\tilde{\psi}^e(\mathcal{I}_{\mathbf{E}^e}) + \tilde{\psi}^c(\epsilon^c) \right]$ is a free energy per unit volume of the intermediate space defined by the range of $\mathbf{F}^c(\mathbf{X})$, and multiplication of this term by J^c gives the free energy per unit volume of the reference space. Further:

(i) ψ_R^e is an elastic energy given by,

$$\tilde{\psi}^e(\mathcal{I}_{\mathbf{E}^e}) = G|\mathbf{E}^e|^2 + \frac{1}{2}\left(K - \frac{2}{3}G\right)(\operatorname{tr}\mathbf{E}^e)^2. \tag{2.68}$$

Here G is the shear modulus, K the bulk modulus, respectively. This free energy is a simple generalization of the classical strain energy function of isotropic linear elasticity to moderately large elastic deformations using the logarithmic strain measure(Anand, 1979).

(ii) We assume that the crazing process gives rise to local disordering which stores energy according to,

$$\tilde{\psi}^c(\epsilon^c) = (1 - \varkappa)\,S^c\epsilon^c, \tag{2.69}$$

with $S^c > 0$ a constant modulus with units of stress representing the craze flow resistance, and $\varkappa$ is positive-valued fraction, such that $\varkappa S^c\epsilon^c$ represents the dissipation due to craze flow, and that the fraction $(1 - \varkappa)\,S^c\epsilon^c$ is stored in the material.[4]

(iii) The positive-valued $g(\mathsf{d}) \geq 0$ *degradation function* is monotonically decreasing,

$$g'(\mathsf{d}) \leq 0, \tag{2.70}$$

and satisfies

$$g(0) = 1, \quad g(1) = 0, \quad \text{and} \quad g'(1) = 0. \tag{2.71}$$

A widely-used degradation function is (cf., e.g., Bourdin et al., 2000; Miehe et al., 2010a; Ambati et al., 2015),

$$g(\mathsf{d}) = (1 - \mathsf{d})^2; \tag{2.72}$$

we adopt it here.[5]

(iv) In order to account for gradient effects for the damage we have included a quadratic term

---

[4]More complicated forms for $\tilde{\psi}^c(\epsilon^c)$ my be chosen, but at this time not much is known about such energy storage mechanisms due to crazing.

[5]In numerical calculations $g(\mathsf{d})$ is modified as

$$g(\mathsf{d}) = (1 - \mathsf{d})^2 + k, \tag{2.73}$$

where $k \approx 0$ is a small positive-valued constant which is introduced to prevent ill-conditioning of the model when $\mathsf{d} = 1$.

dependent the gradient $\nabla \mathsf{d}$,

$$A\,|\nabla \mathsf{d}|^2, \tag{2.74}$$

where A is coefficient with units of energy per unit volume times length-squared.

Thus, combining (2.67), (2.68) and (2.74), the free energy is taken to be given by,

$$\psi_{\mathrm{R}} = g(\mathsf{d})J^c \left[\underbrace{G|\mathbf{E}^e|^2 + \frac{1}{2}\left(K - \frac{2}{3}G\right)(\operatorname{tr}\mathbf{E}^e)^2}_{\tilde{\psi}^e(\mathcal{I}_{\mathbf{E}^e})} + \underbrace{(1-\varkappa)\,S^c\epsilon^c}_{\tilde{\psi}^c(\epsilon^c)} \right] + A\,|\nabla \mathsf{d}|^2. \tag{2.75}$$

Then, by (2.65) the Mandel stress is given by

$$\mathbf{M}^e = g(\mathsf{d})\left[2G\mathbf{E}_0^e + K(\operatorname{tr}\mathbf{E}^e)\mathbf{1}\right]. \tag{2.76}$$

Further, from (2.75), (2.50), and (2.49)$_4$,

$$\pi_{\mathrm{en}} = g(\mathsf{d})\,(1-\varkappa)S^c,$$

$$\varpi_{\mathrm{en}} = g'(\mathsf{d})\,J^c\left(\tilde{\psi}^e(\mathcal{I}_{\mathbf{E}^e}) + \tilde{\psi}^c(\epsilon^c)\right), \tag{2.77}$$

$$\boldsymbol{\xi} = 2A\nabla \mathsf{d}.$$

2.8   Craze flow rule

The spectral decomposition of the Mandel stress $\mathbf{M}^e$ is $\mathbf{M}^e = \sum_{i=1}^{3} \sigma_i\,\hat{\mathbf{e}}_i \otimes \hat{\mathbf{e}}_i$ where $\{\sigma_i|i=1,2,3\}$ are the principal values and and $\{\hat{\mathbf{e}}_i|i=1,2,3\}$ are the principal directions of $\mathbf{M}^e$. We take that the principal stresses to be strictly ordered such that

$$\sigma_1 \geq \sigma_2 \geq \sigma_3.$$

Further, we denote the mean normal stress by

$$\sigma_{\mathrm{M}} \stackrel{\text{def}}{=} \frac{1}{3}(\sigma_1 + \sigma_2 + \sigma_3) > 0. \tag{2.78}$$

37

We postulate that crazing in a material neighborhood can occur only when the maximum principal stress and the mean normal stress are positive:

$$\dot{\epsilon}^c = \begin{cases} > 0 \text{ possible} & \text{if } \sigma_1 > 0 \quad \text{and} \quad \sigma_M = \frac{1}{3}(\sigma_1 + \sigma_2 + \sigma_3) > 0, \\ 0 & \text{otherwise.} \end{cases} \tag{2.79}$$

If $\dot{\epsilon}^c = 0$ then there is no need to specify a consitutive equation for π_{dis}, while when $\dot{\epsilon}^c > 0$ we assume that the dissipative microforce π_{dis} is given by a constitutive equation of the form

$$\pi_{\text{dis}} = \underbrace{g(\mathbf{d})J^c \varkappa S^c}_{\text{resistance to craze flow}} \geq 0, \tag{2.80}$$

In (2.80),

$$S^c > 0, \tag{2.81}$$

is a constant modulus with units of stress representing the craze flow resistance, and $\varkappa \in (0,1)$ is positive-valued fraction such that $g(\mathbf{d})J^c \varkappa S^c \dot{\epsilon}^c$ represents the dissipation due to craze flow, and so that the dissipation inequality $(2.53)_2$ is satisfied. Thus from $(2.77)_1$ and (2.80) the microforce π is given by

$$\pi = \underbrace{g(\mathbf{d})J^c(1 - \varkappa)S^c}_{\pi_{\text{en}}} + \underbrace{g(\mathbf{d})J^c \varkappa S^c}_{\pi_{\text{dis}}} = g(\mathbf{d})J^c S^c. \tag{2.82}$$

Further, we assume that the direction $\mathbf{m}$ for craze extension coincides with the maximum principle stress direction,

$$\mathbf{m} \equiv \hat{\mathbf{e}}_1. \tag{2.83}$$

That is, we assume that

- *the craze flow direction $\mathbf{N}^c$ is parallel to and points in the same direction as the direction of the eigen projection-tensor $\hat{\mathbf{e}}_1 \otimes \hat{\mathbf{e}}_1$ corresponding to the maximum principal value σ_1 of $\mathbf{M}^e$:*

$$\mathbf{N}^c = \hat{\mathbf{e}}_1 \otimes \hat{\mathbf{e}}_1. \tag{2.84}$$

In this case the *resolved tensile stress* σ appearing in (2.37) is

$$J^c \mathbf{M}^e : \mathbf{N}^c = J^c \sigma_1. \tag{2.85}$$

Thus, from the microforce balance (2.36) and the constitutive equation (2.82), we obtain the following *strength relation for craze flow*,

$$\sigma_1 = g(\mathbf{d}) S^c \quad \text{when} \quad \dot{\epsilon}^c > 0. \tag{2.86}$$

We may rewrite (2.86) as

$$f = 0 \quad \text{when} \quad \dot{\epsilon}^c > 0, \tag{2.87}$$

where

$$f \overset{\text{def}}{=} \sigma_1 - g(\mathbf{d}) S^c, \tag{2.88}$$

represents a *yield function* for craze flow. Equation (2.87) implies that a necessary condition for $\dot{\epsilon}^c > 0$ is that

$$f = 0; \tag{2.89}$$

we assume here that this condition is also sufficient for $\dot{\epsilon}^c > 0$. This means that craze flow occurs only when (2.89) holds. Equivalently $\dot{\epsilon}^c = 0$, and no craze flow occurs when

$$f < 0. \tag{2.90}$$

Thus, in our rate-independent model for craze flow we have,

$$\dot{\epsilon}^c \geq 0, \qquad f \leq 0, \qquad \dot{\epsilon}^c f = 0, \tag{2.91}$$

which are the Kuhn-Tucker conditions associated with rate-independent craze flow. It may be shown that in the rate-independent theory,

$$\text{if } \dot{\epsilon}^c > 0, \text{ then } f = 0 \text{ and } \dot{f} = 0, \tag{2.92}$$

which is known as the *consistency condition*. The consistency condition may be used to determine

the value of $\dot{\epsilon}^c$ when it is non-zero.

Finally, using (2.84) and (2.14) with the consistency condition (2.92) serving to determine $\dot{\epsilon}^c$ when it is non-zero. the evolution equation for $\mathbf{F}^c$ is then taken to be given by

$$\dot{\mathbf{F}}^c = \mathbf{D}^c \mathbf{F}^c, \qquad \text{with} \qquad \mathbf{D}^c = \dot{\epsilon}^c \hat{\mathbf{e}}_1 \otimes \hat{\mathbf{e}}_1 \qquad (2.93)$$

2.9 Evolution equation for the damage variable d

Recall the reduced dissipation inequality $(2.53)_3$,

$$\varpi_{\text{dis}} \dot{\mathsf{d}} \geq 0. \qquad (2.94)$$

As a special constitutive equation for ϖ_{dis} we take it to be given by,

$$\varpi_{\text{dis}} = \alpha + \zeta \dot{\mathsf{d}}, \qquad (2.95)$$

with α given by

$$\alpha = 2(1 - \mathsf{d})\psi_{\text{cr}} + 2\psi_* \mathsf{d} > 0, \quad \text{with} \quad \psi_{\text{cr}} > 0 \quad \text{and} \quad \psi_* > 0, \qquad (2.96)$$

and

$$\zeta > 0 \text{ is a constant kinetic modulus,} \qquad (2.97)$$

so that the dissipation inequality (2.94) is satisfied, that is

$$\left(\alpha + \zeta \dot{\mathsf{d}}\right) \dot{\mathsf{d}} > 0 \quad \text{whenever} \quad \dot{\mathsf{d}} > 0, \qquad (2.98)$$

Note from (2.98) that in the rate-independent limit ($\zeta = 0$), the energy dissipated per unit volume as d increases from 0 to 1 is given by

$$\left[2(\mathsf{d} - \frac{1}{2}\mathsf{d}^2)\psi_{\text{cr}} + \psi_* \mathsf{d}^2\right]_0^1 = \psi_{\text{cr}} + \psi_*. \qquad (2.99)$$

Thus $(\psi_{\text{cr}} + \psi_*)$ represents a contribution to the energy per unit volume dissipated during dam-

age growth.[6] As we shall see shortly, damage will be presumed to initiate when the free energy $\left(\tilde{\psi}^e(\mathcal{I}_{\mathbf{E}^e}) + \tilde{\psi}^c(\epsilon^c) \right)$ reaches a value equal to ψ_{cr}. A further increase in the deformation results in an increasing value of d, and ψ_* represents an additional energy dissipated in the fracture process as d increases from 0 to 1.

From (2.51), (2.77), and (2.95) the scalar microstress ϖ and the vector microstress $\boldsymbol{\xi}$ are given by the thermodynamically consistent constitutive equations

$$\varpi = \underbrace{-2(1-\mathsf{d})\,J^c\left(\tilde{\psi}^e(\mathcal{I}_{\mathbf{E}^e}) + \tilde{\psi}^c(\epsilon^c)\right)}_{\text{energetic}} + \underbrace{2(1-\mathsf{d})\psi_{\mathrm{cr}} + 2\psi_*\mathsf{d} + \zeta\,\dot{\mathsf{d}}}_{\text{dissipative}}, \qquad \text{and} \qquad \boldsymbol{\xi} = \underbrace{2A\nabla\mathsf{d}}_{\text{energetic}}\,.$$

$$(2.100)$$

These constitutive relations and the microforce balance (2.38), viz.

$$\mathrm{Div}\,\boldsymbol{\xi} - \varpi = 0,$$

yield the following evolution equation for d,

$$\zeta\dot{\mathsf{d}} = 2(1-\mathsf{d})\,\psi_0 - 2(1-\mathsf{d})\psi_{\mathrm{cr}} - 2\psi_*\mathsf{d} + 2A\,\Delta\mathsf{d}, \qquad (2.101)$$

where

$$\psi_0 \stackrel{\text{def}}{=} J^c\left(\tilde{\psi}^e(\mathcal{I}_{\mathbf{E}^e}) + \tilde{\psi}^c(\epsilon^c)\right) \qquad (2.102)$$

represents an undamaged free energy.

Consider the rate-independent limit, $\zeta = 0$, in the absence of the gradient effects, $\Delta\mathsf{d} = \mathbf{0}$. Then the microforce balance (2.101) during the damaging process $\dot{\mathsf{d}} > 0$ requires that

$$2(1-\mathsf{d})\,(\psi_0 - \psi_{\mathrm{cr}}) - 2\psi_*\mathsf{d} = 0, \qquad (2.103)$$

which gives

$$\mathsf{d} = \frac{(\psi_0 - \psi_{\mathrm{cr}})}{\psi_* + (\psi_0 - \psi_{\mathrm{cr}})}. \qquad (2.104)$$

Note that (2.104) shows that $\mathsf{d} > 0$ only if $\psi_0 > \psi_{\mathrm{cr}}$. Thus, to ensure that $\mathsf{d} \in [0,1]$ we use the

---

[6]There is of course an additional "viscous" energy dissipation due to the contribution from the term involving ζ.

Macauley bracket,

$$\langle x \rangle = \begin{cases} 0, & x < 0, \\ x, & x \geq 0, \end{cases}$$

and rewrite (2.104) as

$$\mathsf{d} = \frac{\langle \psi_0 - \psi_{\mathrm{cr}} \rangle}{\psi_* + \langle \psi_0 - \psi_{\mathrm{cr}} \rangle}, \tag{2.105}$$

or in a form similar to (2.103) as

$$2(1 - \mathsf{d}) \langle \psi_0 - \psi_{\mathrm{cr}} \rangle - 2\psi_* \mathsf{d} = 0. \tag{2.106}$$

Next, eq. (2.105) in turn gives

$$\dot{\mathsf{d}} = \frac{\psi_* \overline{\langle \psi_0 - \psi_{\mathrm{cr}} \rangle}}{(\psi_* + \langle \psi_0 - \psi_{\mathrm{cr}} \rangle)^2}. \tag{2.107}$$

Then, in order to satisfy the irreversibility constraint, $\dot{\mathsf{d}} \geq 0$, from (2.107) we see that we must require that

$$\overline{\langle \psi_0 - \psi_{\mathrm{cr}} \rangle} \geq 0. \tag{2.108}$$

That is, the damage "driving force" $\langle \psi_0 - \psi_{\mathrm{cr}} \rangle$ must be a *montonously increasing function* of time. This requirement is satisfied if we replace $\langle \psi_0 - \psi_{\mathrm{cr}} \rangle$ in (2.106) with the monotonically increasing history field function (cf., Miehe et al., 2015):

$$\mathcal{H}(t) \overset{\text{def}}{=} \max_{s \in [0,t]} \left[\langle \psi_0(s) - \psi_{\mathrm{cr}} \rangle \right]. \tag{2.109}$$

We further impose the requirement that the craze strain must exceed a critical value, ϵ_{cr}^c before the history field may evolve and damage process may initiate.

$$\mathcal{H}(t) \overset{\text{def}}{=} \begin{cases} 0, & \text{if } \epsilon^c < \epsilon_{\mathrm{cr}}^c \\ \max_{s \in [0,t]} \left[\langle \psi_0(s) - \psi_{\mathrm{cr}} \rangle \right], & \text{otherwise} \end{cases} \tag{2.110}$$

Finally, reinstating the rate-dependence and the dependence on $\Delta \mathsf{d}$, as in (2.101), the evolution of

d is then governed by the partial differential equation,

$$\zeta \dot{\mathsf{d}} = 2(1 - \mathsf{d})\,\mathcal{H} - 2\psi_*\mathsf{d} + 2A\,\Delta\mathsf{d}, \quad \text{with}$$

$$\mathcal{H} \stackrel{\text{def}}{=} \begin{cases} 0, & \text{if } \epsilon^c < \epsilon^c_{\text{cr}} \\[2ex] \max_{s \in [0,t]}\left[\langle \psi_0(s) - \psi_{\text{cr}}\rangle\right], & \text{otherwise} \end{cases} \quad \text{where} \tag{2.111}$$

$$\psi_0 \stackrel{\text{def}}{=} J^c\left[\left(G|\mathbf{E}^e|^2 + \frac{1}{2}\left(K - \frac{2}{3}G\right)(\text{tr}\,\mathbf{E}^e)^2\right) + (1 - \varkappa)S^c\epsilon^c\right].$$

The evolution equation (2.125) for d is similar to the evolution equation for d in the papers by Miehe et al. (cf., e.g., Miehe et al., 2010a,b, 2015, 2016) on phase field modeling of fracture. Indeed if we take the energetic term A which is associated with the damage-gradient contribution to the free energy in (2.74) to be given by

$$A \equiv \psi_*\ell^2, \tag{2.112}$$

where $\ell > 0$ is an internal length scale which controls the width of zones across which the damage varies rapidly, then $(2.111)_1$ reduces to

$$\zeta \dot{\mathsf{d}} = 2(1 - \mathsf{d})\,\mathcal{H} - 2\psi_*(\mathsf{d} - \ell^2\,\Delta\mathsf{d}). \tag{2.113}$$

which is of a form identical to that in the work of Miehe and co-workers (cf., e.g., Miehe et al., 2015, eq. (53)). *However, the details of our derivation differ in may respects from the derivations given in the papers by these authors.* Differences of particular importance are:

- We allow for a small amount of inelastic craze-like deformation when the maximum principle tensile stress reaches a critical value $S^c > 0$, which we call the craze strength.

- Craze inelasticity is allowed to occur only when the maximum principal stress is positive. There is no need in our theory to decompose the free energy into "positive" and "negative" parts to avoid cracking under "compressive" states of strain, as done in most existing theories for phase-field modeling of fracture.

- We do not a-priori invoke the purely geometric ideas of approximating a sharp-crack topology by a damage field d and a length-scale ℓ.

43

- Our theory contains a material parameter ψ_{cr} which sets a level of energy that must be exceeded before damage initiates.

- The value of the parameter A which appears in the contribution $A\,|\nabla\mathsf{d}|^2$ to the free energy (2.75) in our theory is constitutively taken to have a value $A = \psi_*\ell^2$; we do so in order to make connection with the work of Miehe and co-workers. The term $A\,|\nabla\mathsf{d}|^2 = \psi_*\ell^2|\nabla\mathsf{d}|^2$ is *energetic* in our theory since it appears in the free energy (2.75), and therefore the term $2\psi_*\ell^2\Delta\mathsf{d}$ in eq. (2.125) is also *energetic* and not *dissipative* — as is commonly assumed in the literature by many including Miehe and co-workers.

- The value of the strength parameter S^c in our theory is not related to the elastic Young's modulus E, a toughness G_c, and the length scale ℓ — as in most existing phase-field theories of fracture (cf., e.g., Pham et al., 2017). In our theory the material strength is controlled directly by S^c.

- The parameter ℓ is a suitable gradient regularization parameter which may be *independently* prescribed based on physical considerations of the microstructure and computational-tractability.

2.10 Summary

The theory formulated above is summarized below :

2.10.1 Constitutive equations

1. *Free energy*

   The free energy is taken to be given by,

   $$\psi_{\mathrm{R}} = g(\mathsf{d})\psi_0 + \psi_*\ell^2\,|\nabla\mathsf{d}|^2, \quad \text{with}$$

   $$\psi_0 = J^c\underbrace{\left[G|\mathbf{E}^e|^2 + \frac{1}{2}\left(K - \frac{2}{3}G\right)(\operatorname{tr}\mathbf{E}^e)^2 + (1 - \varkappa)\,S^c\epsilon^c \right]}_{\text{``undamaged'' energy}}. \tag{2.114}$$

   Here:

(i) $G, K > 0$ are the shear and bulk moduli, respectively.

(ii) $S^c \epsilon^c$ represents an inelastic work expended due to crazing and $\varkappa$ a fraction in the range $\varkappa \in (0, 1)$. We assume that the fraction $\varkappa S^c \epsilon^c$ is dissipated, while the balance $(1 - \varkappa) S^c \epsilon^c$ is stored in the material due to craze-disordering,

$$S^c \epsilon^c = \underbrace{\varkappa S^c \epsilon^c}_{\text{energy dissipated due to crazing}} + \underbrace{(1 - \varkappa) S^c \epsilon^c}_{\text{energy stored due to craze disordering}} . \qquad (2.115)$$

(iii) $g(\mathsf{d}) = (1 - \mathsf{d})^2$ is a monotonically decreasing *degradation function*.

(iv) The parameter ψ_* is an energy per unit volume associated with the evolution of damage, and $\ell > 0$ is a length scale parameter that controls the spread of the diffuse damage zone.

2. *Mandel stress*

The Mandel stress is given by

$$\mathbf{M}^e = J^{c-1} \left(\frac{\partial \psi_{\mathrm{R}}}{\partial \mathbf{E}^e} \right) = g(\mathsf{d}) \left[2G \mathbf{E}_0^e + K (\operatorname{tr} \mathbf{E}^e) \mathbf{1} \right], \qquad (2.116)$$

which is symmetric. The spectral decomposition of the Mandel stress is

$$\mathbf{M}^e = \sum_{i=1}^{3} \sigma_i \, \hat{\mathbf{e}}_i \otimes \hat{\mathbf{e}}_i \quad \text{with} \quad \sigma_1 \geq \sigma_2 \geq \sigma_3, \qquad (2.117)$$

where $\{\sigma_i | i = 1, 2, 3\}$ are the principal values and $\{\hat{\mathbf{e}}_i | i = 1, 2, 3\}$ are the principal directions of $\mathbf{M}^e$. Craze inelasticity will be taken to occur in the maximum principal stress direction $\hat{\mathbf{e}}_1$; cf. eq. (2.118) below.

3. *Evolution equation for* $\mathbf{F}^c$

The evolution of $\mathbf{F}^c$ is taken to be given by,

$$\dot{\mathbf{F}}^c = \mathbf{D}^c\mathbf{F}^c \quad \text{with initial condition} \quad \mathbf{F}^c(\mathbf{X}, 0) = \mathbf{1}, \quad \text{where}$$

$$\mathbf{D}^c = \dot{\epsilon}^c \hat{\mathbf{e}}_1 \otimes \hat{\mathbf{e}}_1, \quad \text{and}$$

$$\dot{\epsilon}^c = \begin{cases} > 0 \text{ possible} & \text{if } \sigma_1 > 0 \quad \text{and} \quad \sigma_{\mathrm{M}} = \frac{1}{3}(\sigma_1 + \sigma_2 + \sigma_3) > 0, \\ 0 & \text{otherwise.} \end{cases} \tag{2.118}$$

Here $\dot{\epsilon}^c \geq 0$ is craze strain-rate, which is determined, as discussed below, in a manner similar to that in classical theories of rate-independent inelasticity.

With $S^c > 0$ denoting a stress-dimensioned variable representing a resistance to craze flow, we introduce a *yield function*

$$f \stackrel{\text{def}}{=} \sigma_1 - g(\mathbf{d})S^c,$$

and require that

$$f \leq 0, \tag{2.119}$$

which limits the admissible maximum principal stress σ_1. Then, as is standard in rate-independent theories of plasticity, the loading-unloading conditions may be expressed in the Kuhn-Tucker form

$$\dot{\epsilon}^c \geq 0, \quad f \leq 0, \quad \dot{\epsilon}^c f = 0,$$

to which we append the consistency condition

$$\dot{\epsilon}^c \dot{f} = 0 \quad \text{when} \quad f = 0.$$

The consistency condition serves to determine $\dot{\epsilon}^c$ whenever it is not zero. The *craze strain* is defined by

$$\epsilon^c(t) \stackrel{\text{def}}{=} \int_0^t \dot{\epsilon}^c(s)\,ds. \tag{2.120}$$

4. *Evolution equation for the damage variable* d

46

Let

$$\psi_0 \stackrel{\text{def}}{=} J^c \left[\underbrace{\left(G|\mathbf{E}^e|^2 + \frac{1}{2}\left(K - \frac{2}{3}G\right)(\text{tr}\,\mathbf{E}^e)^2\right)}_{\text{elastic energy}} + \underbrace{(1 - \varkappa)S^c \epsilon^c}_{\text{craze disordering energy}} \right], \qquad (2.121)$$

represent a "driving energy" per unit volume for damage growth; cf. eq. (2.114). Then, with $\psi_{\text{cr}}, \epsilon_{\text{cr}}^c$ representing *threshold values* of energy and craze strain respectively for initiation of damage, we define a history loading parameter by

$$\mathcal{H} \stackrel{\text{def}}{=} \begin{cases} 0, & \text{if } \epsilon^c < \epsilon_{\text{cr}}^c \\[2ex] \max_{s \in [0,t]} \left[\langle \psi_0(s) - \psi_{\text{cr}} \rangle \right], & \text{otherwise} \end{cases}, \qquad (2.122)$$

and take the evolution of d to be governed by the partial differential equation,

$$\zeta \,\dot{\mathsf{d}} = 2(1 - \mathsf{d})\,\mathcal{H} - 2\psi_*(\mathsf{d} - \ell^2\,\Delta\mathsf{d}), \qquad (2.123)$$

where $\zeta > 0$ is a (small) viscous regularization parameter.

2.10.2 Governing partial differential equations. Boundary and initial conditions

The governing partial differential equations consist of:

1. The force balance (neglecting body forces and inertia),

$$\text{Div}\,\mathbf{T}_{\text{R}} = \mathbf{0}, \qquad (2.124)$$

where $\mathbf{T}_{\text{R}}$ is the Piola stress. The boundary conditions are

$$\boldsymbol{\chi} = \check{\boldsymbol{\chi}} \quad \text{on} \quad \mathcal{S}_{\boldsymbol{\chi}} \times [0, T], \qquad \mathbf{T}_{\text{R}}\mathbf{n}_{\text{R}} = \check{\mathbf{t}}_{\text{R}} \quad \text{on} \quad \mathcal{S}_{\mathbf{t}_{\text{R}}} \times [0, T],$$

where $\mathcal{S}_{\boldsymbol{\chi}}$ and $\mathcal{S}_{\mathbf{t}_{\text{R}}}$ are complementary subsurfaces of ∂B. To these boundary conditions we append the initial condition $\boldsymbol{\chi}(\mathbf{X}, 0) = \boldsymbol{\chi}_0(\mathbf{X})$ in B.

47

2. Evolution of d,

$$\zeta \dot{\mathbf{d}} = 2(1 - \mathbf{d})\,\mathcal{H} - 2\psi_*(\mathbf{d} - \ell^2\,\Delta\mathbf{d}). \tag{2.125}$$

The boundary conditions for this partial differential equation are taken as

$$\mathbf{d} = 0 \quad \text{on } \mathcal{S}_{\mathbf{d}} \times [0, T], \qquad (\nabla\mathbf{d})\cdot\mathbf{n}_{\mathrm{R}} = 0 \quad \text{on } \mathcal{S}_{\nabla\mathbf{d}} \times [0, T],$$

where $\mathcal{S}_{\mathbf{d}}$ and $\mathcal{S}_{\nabla\mathbf{d}}$ are complementary subsurfaces of ∂B. To this we append the initial condition $\mathbf{d}(\mathbf{X}, 0) = 0$ in B.

2.11 Constitutive response of a single element undergoing homogeneous simple extension

To fix ideas regarding the intrinsic stress-strain response of the material in the absence of the effects of a gradient in the damage field, we first consider the response of a single element in monotonic simple extension under homogeneous plane-strain conditions. The numerically calculated stress-strain response is shown in Fig. 2-1(a). As the strain is increased from zero, the initial response is elastic until a craze strength level S^c is reached at point (i) marked in Fig. 2-1, when inelastic deformation due to crazing is initiated.[7] With further extension the craze strain ϵ^c increases, while the stress-level remains constant at S^c. When the craze strain reaches a critical value ϵ_{cr}^c at point (ii) marked in Fig. 2-1, the undamaged energy ψ_0 (cf. eq. $(2.114)_2$) reaches the threshold energy ψ_{cr} (cf. eq. (2.122)), and damage is initiated. The energy density ψ_{cr} has a contribution from the elastic strain at that point, as well as a fraction of the energy stored due to craze growth between points (i) and (ii). A simple one-dimensional estimate for the energy ψ_{cr} in terms of the parameters $(E, S^c, \epsilon_{\mathrm{cr}}^c, \varkappa)$ is

$$\psi_{\mathrm{cr}} = \frac{S^{c2}}{2E} + (1 - \varkappa)S^c\epsilon_{\mathrm{cr}}^c. \tag{2.126}$$

---

[7]In the civil engineering literature on concrete, the parameter S^c which we have called the the *craze strength*, is usually called the *tensile strength* and denoted by f_t or also sometimes by f_t'.

With increasing deformation as the damage progresses, the value of **d** increases and the stress begins to decay. The shape of the decaying portion of the stress-strain curve in Fig. 2-1(a) is controlled by both the degradation function $g(\mathbf{d}) = (1 - \mathbf{d})^2$ as well as the energy density parameter ψ_* in our model. In all the calculations shown in this thesis we keep the degradation function *fixed*, and increasing or decreasing the value of ψ_* increases or decreases the amount of energy dissipated as **d** increases from zero to unity.[8]
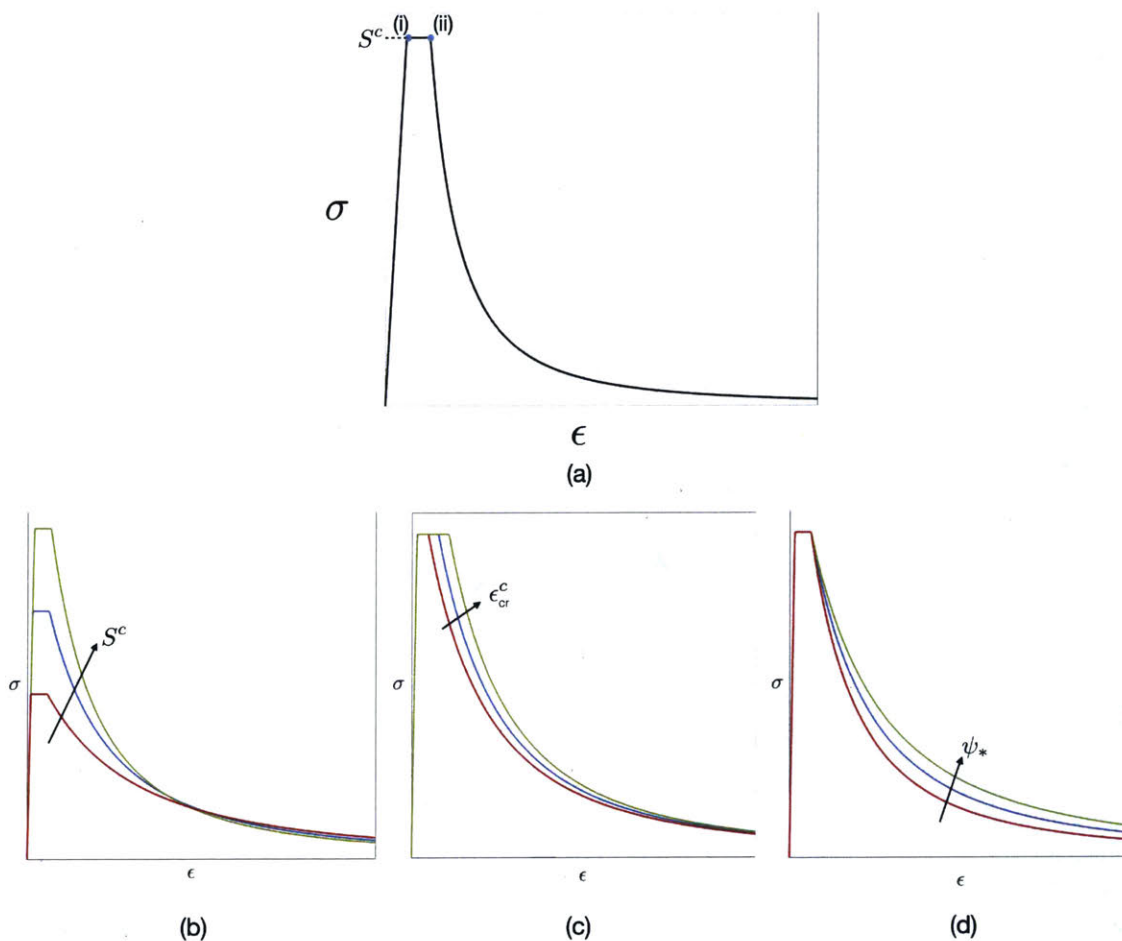
Figure 2-1: (a) Stress-strain response of a single element in monotonic simple extension under homogeneous plane-strain conditions, without gradient-damage effects. Keeping the values of other parameters fixed: (b) shows the effect of varying the value of S^c; (c) shows the effect of varying the value of ϵ_{cr}^c; and (d) shows the effect of varying the value of ψ_*.

---

[8]Although our theory allows for the use of different degradation functions, we refrain from adding complexity to our model by exploring different forms of the degradation function to more closely match experimental data.

Keeping the values of the other material parameters fixed, Fig. 2-1(b), (c), and (d) qualitatively show the effects of increasing the value of S^c, ϵ_{cr}^c, and ψ_*, respectively. Thus the strength and toughness of different quasi-brittle materials may be modeled by suitably varying the values of these parameters. For strain-softening materials the length scale ℓ in our gradient theory also has a major effect on the softening response. We discuss this matter in the next chapter in section 3.1, where we consider the inhomogeneous deformation in a direct tension test on concrete.

We wish to emphasize here the distinction between the craze-type inelasticity (that we have used here) and classical shear-yield plasticity. Although our constitutive response, with a constant stress at the peak load appears analogous to the behavior of a perfectly-plastic metallic material, the two processes are fundamentally different. Classical shear-yield plasticity in metals is based on plastic incompressibility and the plastic deformation is isochoric ; however, crazing is a dilational form of inelasticity which accommodates volume changes that might appear within the RVE due to the opening of several micro-cracks.
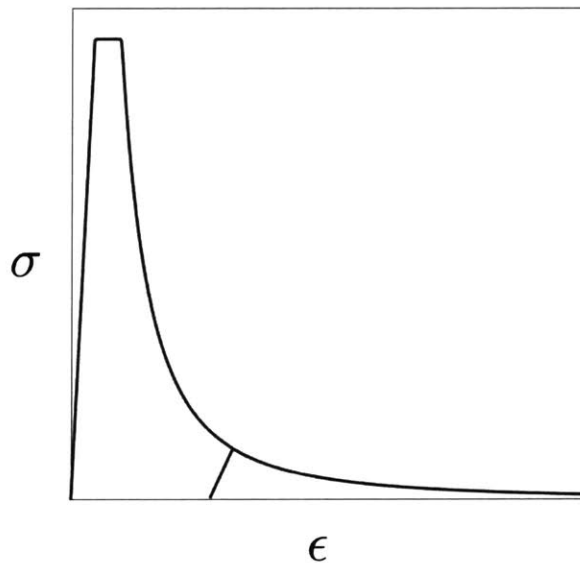
Figure 2-2: Single-element stress-strain response with an unload-reload excursion.

Before closing this section we show the unloading-reloading response of the model. We sub-

jected a single element to extension with an unload-reload excursion in the decaying region of the stress-strain curve. The corresponding stress-strain curve is shown in Fig. 2-2. The unloading branch shows a linear response corresponding to elastic unloading but with a reduced modulus because of the damage. As expected, the intercept of the unloading branch on the strain axis corresponds to the inelastic craze strain ϵ^c at the point on the decay curve from where the unloading process was initiated.

To contrast against the existing phase-field models in the literature for ideally-brittle materials, as in Miehe et al. (2010a), we discuss the effect of craze inelasticity on the behavior. Suppressing crazing in our model, we have an elastic-damage model analogous to Miehe et al.. The single element load-unload response without craze inelasticity is shown in fig.2-3. In the absence of any inelastic mechanisms, damage initiates at the peak followed by decay with progressing damage. A major point of deviation is the unloading characteristic where upon unloading the specimen does not show any permanent set, i.e. unloading response intercept on the strain axis is zero. This is because the deformation is purely elastic.
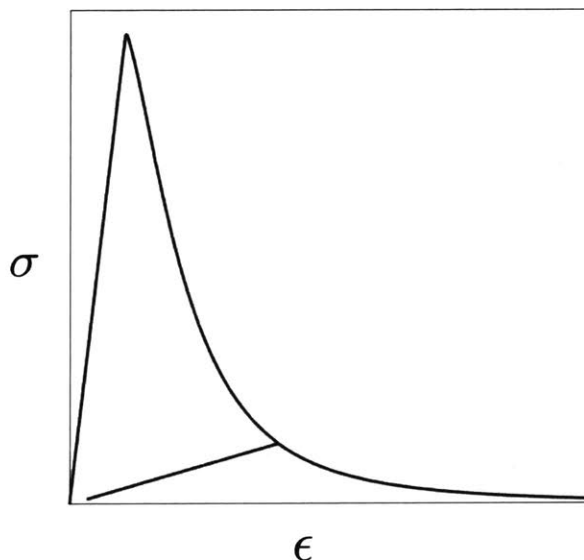
Figure 2-3: Single-element stress-strain response for an elastic-damage model with an unload-reload excursion.

Physically, with the macroscopic deformation of the specimen there is some associated open-

ing of the micro-cracks in concrete. Beyond the onset of damage, it is reasonable to expect that the opening of these several micro-cracks is not completely reversible, i.e., when the load on a damaged concrete specimen is fully removed, micro-crack closure does not necessarily occur. This leads to some unrecovered macroscopic deformation which is associated with some inelastic processes taking place within the material. This is supported by several experiments performed by van Mier and co-workers. Figure 2-4, taken from Schlangen and van Mier (1992) shows the load-displacement curve with several unload-load excursions. Unloading the specimen does not lead to complete recovery of the displacement indicating that some inelastic mechanism are operative during the deformation process. It is based on this type of evidence that we have allowed for some dilational craze-inelasticity before the commencement of damage in order to obtain a response as in fig.2-2 instead of that in fig.2-3
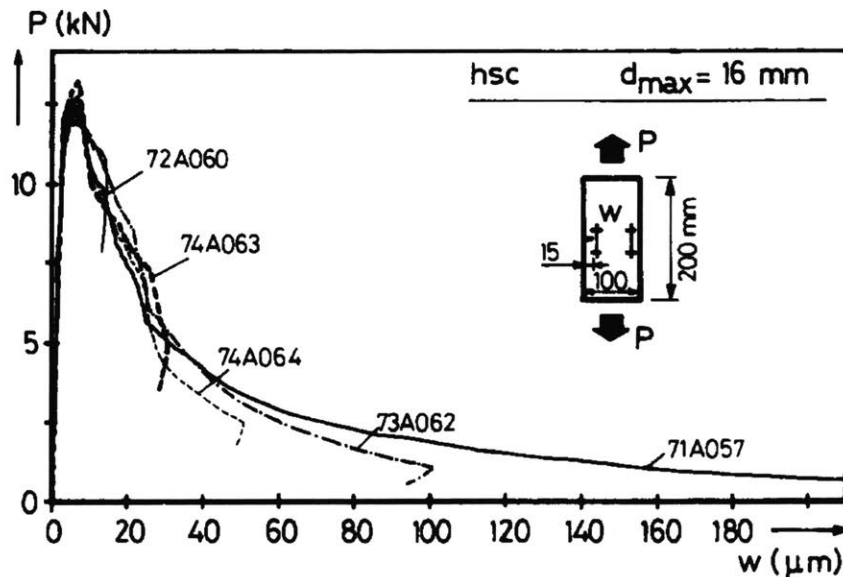
Figure 2-4: Load-crack opening diagram of a single edge notched high strength concrete. Taken from Schlangen and van Mier (1992)

2.12 Material parameters

Before applying the theory to model concrete, we recall that the material parameters in our theory are:

(a) The elastic shear and bulk moduli, G and K. Or equivalently, using the standard relations of isotropic linear elasticity, the Young's modulus E and the Poisson's ratio ν.

(b) The craze strength parameter, $S^c > 0$.

(c) A parameter $\varkappa \in (0, 1)$, such that $(1 - \varkappa)S^c \epsilon^c$ represents the amount of energy per unit volume stored due to crazing.

(d) A parameter ϵ_{cr}^c which represents a critical craze strain which in turn determines an energy ψ_{cr} that must be reached for damage to initiate.

(e) A parameter $\psi_* > 0$ which represents a contribution to the energy dissipated as damage grows from zero to unity.

(f) A length scale parameter, $\ell > 0$, which controls the spread of the diffuse damage zone.

(g) A parameter $\zeta > 0$, which is a small viscous regularization parameter for the evolution of damage.

In the numerical simulations of the different experiments that we consider in the following chapter we have used:

- A constant value of $\varkappa = 0.7$. The precise value of $\varkappa$ is not known. In choosing a value of $\varkappa = 0.7$, we are guided by experience with theories of metal plasticity where a large fraction $\varkappa$ of the inelastic work is dissipated, and a small fraction $(1 - \varkappa)$ stored in the material. Further, our numerical experiments show that a value of $\varkappa = 0.7$ ensures that in the expression (2.121) for the "driving energy" for damage growth, ψ_0, the elastic energy term does not overwhelm the craze-disordering term $(1 - \varkappa)S^c \epsilon^c$. It is possible to use values of $\varkappa$ in the range $\varkappa \in (0.6, 0.8)$, but then the other material parameters would have to be suitably adjusted to obtain similar load-displacement curves. In this thesis we keep the value of this parameter fixed at $\varkappa = 0.7$.

- A constant value of the viscous-regularization parameter $\zeta = 40\text{kPa-s}$.[9] We have chosen this value so that it has only a minor effect on the load-displacement curves in our simulations, while imparting stability to our numerical solution scheme across the various cases in consideration in this thesis.

The experimental data considered in the next chapter is taken from several different publications in which the experiments were performed on different concretes. Because of the inherent variability of the composition and microstructure of different concretes, the calibrated values of the Young's modulus E, the craze strength S^c, and the critical value of the craze strain ϵ^c_{crit} vary quite a bit from one material to another. We discuss the special role of the values for the energy ψ_* and the gradient length scale ℓ in Section 3.1.1.

---

[9]This value is of the same order as that used by Miehe et al. (2010b).

Chapter 3

Application to concrete fracture

In this chapter we demonstrate the capability of our theory and its numerical implementation to reproduce the macroscopic failure response of concrete in several technically relevant geometries reported in the literature. Specifically, we simulate the fracture of concrete in: (i) a direct tension test on a symmetric double-notched specimen; (ii) several symmetrically loaded un-notched and notched three-point bend tests of various specimen sizes; (iii) asymmetrically loaded three-point and four-point notched bend specimens; and finally (iv) an L-shaped panel test without a notch.

3.1   Direct tension test

Even though it is well-known that because of strain-softening the deformation in a direct tension experiment is not homogeneous, such a test is often considered a fundamental experiment to characterize the tensile softening and fracture response of concrete. Such experiments are difficult to perform, and the first set of carefully-controlled, stable tension experiments to obtain the softening response of concrete were conducted in a stiff testing machine by Petersen (1981). Due to the inherent heterogeneity of concrete, homogenous or even slightly tapered tension specimens lead to multiple cracking, and therefore the results form such experiments are not very informative. Hence, symmetric double-notched tension specimens, similar to those shown schematically in Fig. 3-1(a), are often used to characterize the tensile behavior of concrete (Bazant and Planas, 1998).
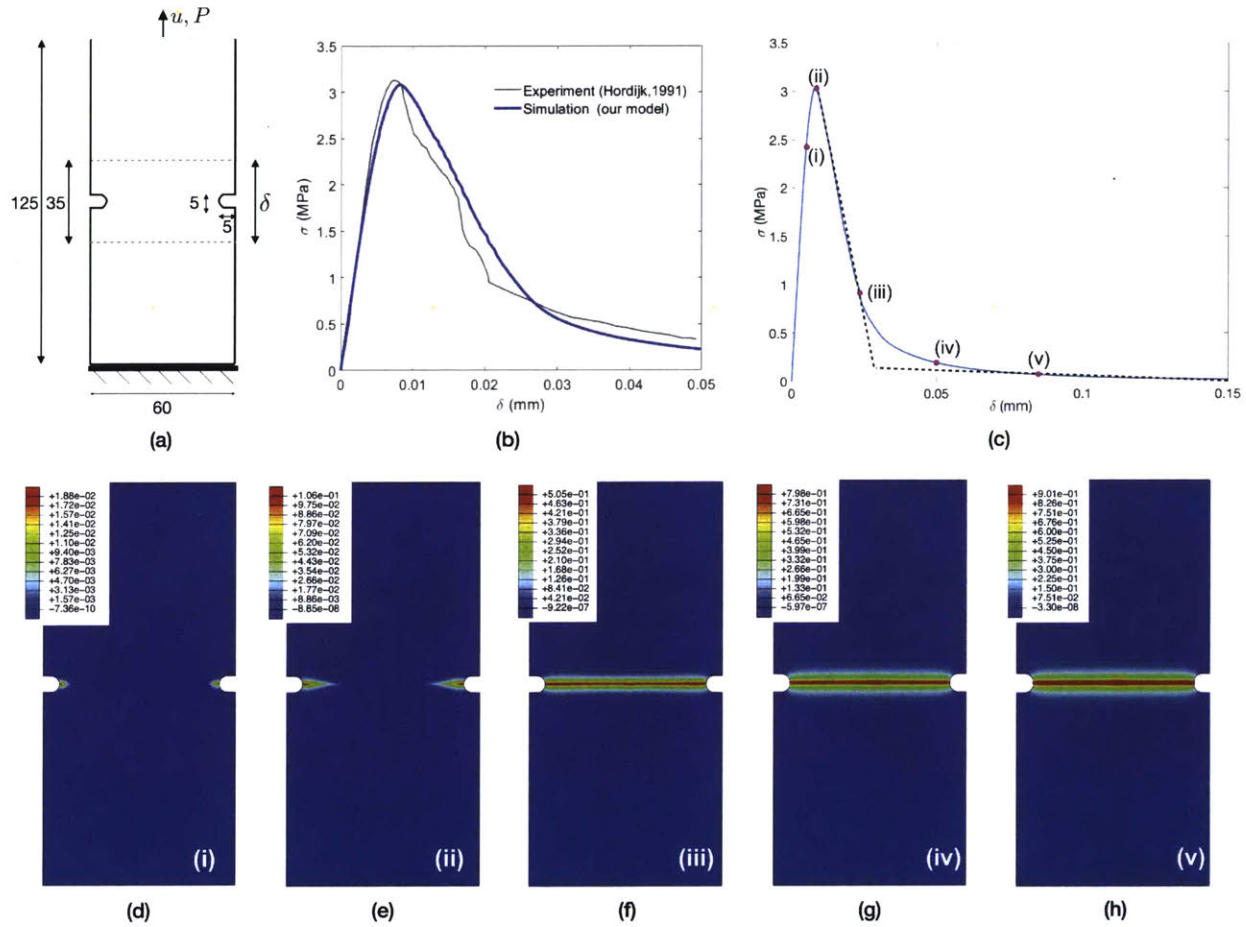
Figure 3-1: (a) Schematic of the geometry of the direct tension specimen; dimensions in mm. (b) Comparison of the experimental σ-δ response (gray line) with the numerically-calculated result (blue) line. (c) The numerically calculated σ-δ response to larger values of δ, showing a bilinear approximation. (d) through (h) Contours of the damage variable d at points (i) through (v) marked on the σ-δ curve in (c).

In this section we use representative data from one such experiment for a concrete reported by Hordijk (1991) in his Ph.D. thesis. The particular specimen that we focus on had an of overall dimension 125×60 mm in the plane, with two symmetric notches each of width and depth of 5mm, and an out-of-plane thickness of 50 mm. The average displacement δ across the notches was obtained by measurements from several extensometers over a gage length of 35 mm spanning the notches, as indicated in Fig. 3-1(a). The nominal stress σ (load P divided by the minimum cross-sectional area) versus the displacement δ reported by (Hordijk, 1991, Fig. 5.6b) is shown in Fig. 3-1(b) as the gray line . We have simulated such an experiment and adjusted the material parameters in our theory

56

to match the σ-δ response reported by Hordijk (1991). The numerically-calculated response is also shown in Fig. 3-1(b) as the blue curve. The material parameters used to obtain the fit are given in Table 3.1. Given the inherent scatter in the experimental data, our model captures the peak and the decaying portion of the σ-δ response quite well.

Table 3.1: Material parameters for the direct tension test simulation

E, GPa	ν	S^c, MPa	$\varkappa$	ϵ^c_{crit}	ψ_*, kJ/m^3	ℓ, mm	ζ, kPa-s
18	0.2	3.2	0.7	5.3×10^{-4}	4.0	2	40

Fig. 3-1(c) shows the numerically calculated σ-δ response to larger values of δ. Figs. 3-1(d) through (f) show contours of the damage variable **d** at points (i) through (v) marked on the σ-δ curve in Fig. 3-1(c). Note from Fig. 3-1(d) that damage starts well before the maximum tensile stress is reached at point (ii). Further the σ-δ curve in Fig. 3-1(c) shows that even at relatively large values of $\delta = 0.15$mm $= 150\,\mu$m, the stress has not completely decayed to zero — the specimen still shows some stress-carrying capacity. This is commensurate with numerous experimental measurements on concrete shown in Fig. 6.4 of Hordijk (1991).

Concrete shows a gradual degradation of modulus prior to the peak load, and this reflects the fact that in the region ahead of the notch-tips crazing and damage accumulates before a major localization happens. It is important to note that this physically realistic macroscopic response is predicted by our model in a multi-element simulation of an inhomogeneous direct-tension test, even though in the underlying homogeneous constitutive response of a single element we have allowed for a small amount of craze strain $\epsilon^c_{\text{crit}} = 5.3 \times 10^{-4}$. That is,

- the physically realistic macroscopic response of a direct tension test simulation of concrete predicted by our model is not very sensitive to the existence of a craze strain in the response of a single element, as long as the craze strain is small, $\epsilon^c_{\text{crit}} \sim \mathcal{O}(10^{-4})$.

Remark. The dashed lines in Fig. 3-1(c) shows that the σ-δ curve may be approximated by two straight lines, a sharp initial descent beyond the peak followed by a long slowly decaying tail. Such an approximation is often made for ease of analysis in bilinear cohesive-crack models of concrete (cf., e.g., Bazant and Planas, 1998; Hoover and Bazant, 2014) . We do not need to make such an approximation in our continuum model and its numerical implementation. $\square$

3.1.1 The gradient length scale ℓ and its relation to the parameter ψ_*

We begin by recalling that the length scale ℓ appears in our gradient-damage theory — in concert with the dependence on $|\nabla\mathsf{d}|^2$ and the energy ψ_* — in the contribution $\psi_*\ell^2|\nabla\mathsf{d}|^2$ to the free energy in eq. (2.114).

In choosing a value for the length scale ℓ for the direct tension test simulations we were guided by the following considerations:

(i) The experimental result of Hordijk (1991) show that the relative displacement had a value of $\delta \approx 0.15$mm before the material lost its stress-carrying capacity, cf. Fig. 3-1(c). So we expected that a value of ≈ 0.15 mm might be an approximate lower bound to the value of ℓ.

(ii) The expectation that the width of the fracture process zone $\approx 2\ell$, would be of the same order as the notch-width of 5 mm.

(iii) That the aggregate size in concrete was ≈ 2 to 5 mm.[1]

Based on these considerations we chose a value of $\ell = 2$ mm and arrived at a value of $\psi_* = 4\text{kJ/m}^3$, together with the other material parameters listed in Table 3.1, from our curve-fitting exercise.
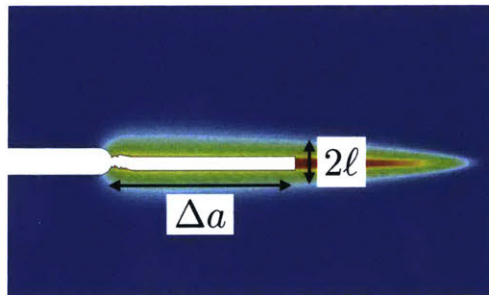
Figure 3-2: A contour plot of the damage variable d in the process zone at a notch tip, showing the width of the process zone $\approx 2\ell$, and the amount of crack extension $\approx \Delta a$. To visualize the amount of crack extension the finite elements with values of $\mathsf{d} > 0.9$ have not been plotted.

Fig. 3-2 shows a contour plot of the damage variable d in a representative process zone at a notch tip. To visualize the fully-damaged region or the amount of crack extension, the finite elements with values of $\mathsf{d} > 0.9$ have not been plotted. In this figure we have marked the width of the process zone as $\approx 2\ell$, and the amount of crack extension as $\approx \Delta a$. Recall that in our theory the parameter

---

[1]The maximum aggregate size in concrete can sometimes get as large as 10 mm or even larger.

ψ_* represents (a portion of) the energy per unit volume dissipated as the damage variable increases form zero to unity. Thus the energy dissipated in the volume ($2\ell \times \Delta a \times$ unit depth) is proportional to ($\psi_* \times \ell \times \Delta a$), and hence

- the energy dissipated per unit area of crack extension is proportional to ($\psi_* \times \ell$).

In Table 3.1 the values for ℓ and ψ_* were taken as $\ell = 2\,\mathrm{mm}$ and $\psi_* = 4\mathrm{kJ/m}^3$, respectively. However, as indicated by our simple dimensional analysis above, if we were to choose values of ℓ and ψ_* such that the product

- ($\psi_* \times \ell$) is kept constant,

then the decaying portion of the σ-δ curve should not be significantly affected by variations in the value of ℓ. This is indeed borne out by our numerical simulations shown in Fig. 3-3, where we show σ-δ curves for the direct tension tests with the values of all other material parameters fixed, but the values of ℓ varying between $0.5\,\mathrm{mm}$ and $5\,\mathrm{mm}$ while keeping the product

$$(\psi_* \times \ell) = 8\mathrm{J/m}^2 \quad \text{constant.}$$
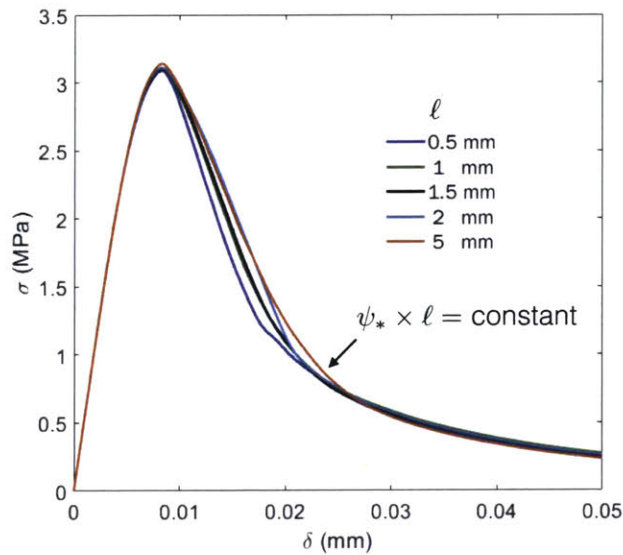
Figure 3-3: Variation of the σ-δ curve using different values of ℓ and ψ_* keeping $\psi_* \times \ell = $ constant.

Some remarks:

1. We consider ℓ as an adjustable regularization parameter in our gradient damage theory. The value of ℓ may be chosen in a suitable physically realistic range. If the value of ℓ is varied in this range and correspondingly the value of ψ_* is adjusted such that $(\psi_* \times \ell)$ is held constant, then the resulting σ-δ response will not be substantially altered.

2. The value of the constant $(\psi_* \times \ell)$ will of course be different for different concretes, but we expect it to have a value of $\approx 10\,\mathrm{J/m^2}$, which represents an intrinsic portion of the toughness of the material. For reference, the value of the critical energy release rate for brittle fracture of soda-lime glass is $\mathcal{G}_c \approx 10\,\mathrm{J/m^2}$. There is of course a major additional contribution to the overall toughness of concrete due to the distributed inelastic deformation of the material due to crazing prior to and during the process of craze-breakdown and its progression to final failure. It is the energy dissipated due to crazing that makes the material "quasi-brittle".

3. This scaling further suggests that in finite element calculations a small but computationally-tractable mesh size h_e may be selected for macroscopic-dimensioned specimens, and a suitably large value of $\ell \gtrsim 5 \times h_e$ may be chosen, and the value of ψ_* suitably adjusted so that $(\psi_* \times \ell) = $ constant for a particular concrete. We take this pragmatic approach for the numerical simulations shown in the remaining sections of this chapter.

$\square$

3.1.2 Mesh insensitivity

$h_e \sim 300\ \mu$m $\qquad$ $h_e \sim 200\ \mu$m $\qquad$ $h_e \sim 150\ \mu$m $\qquad$ $h_e \sim 100\ \mu$m
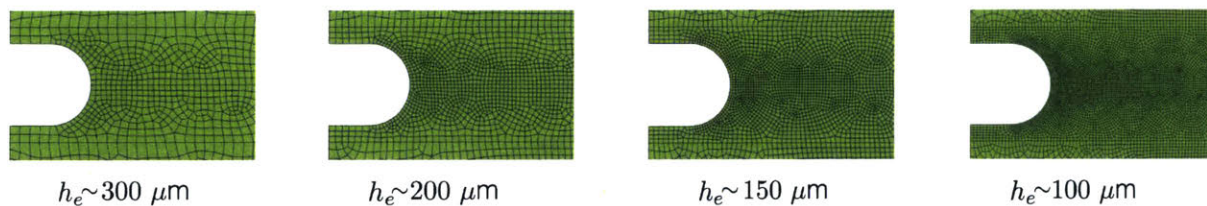
Figure 3-4: Meshes of varying resolution in the damage zone for the direct tension specimen

In this section we illustrate the above simulation results are mesh objective due to the 'regularized' gradient damage theory as suggested in the introductory chapter. We consider four different meshes

with the mesh sizes $h_e \in \{100, 150, 200, 300\}\mu$m in the damage zone. The mesh around the notch for the four different resolutions are shown in fig.3-4. The overall geometry and the boundary conditions are all identical to that described above.

The damage contours around the notch for the different mesh resolutions in consideration are shown in fig.3-5(a). Due to the regularization —gradient damage — the damage zone width remains invariant for the meshes, thus independent of the element size. The resulting nominal stress-displacement plots for the different mesh resolutions are shown together in fig.3-5(b). The responses are nearly coincident with the exception of the coarsest mesh in a small region post-peak indicating that the curves are converging to identical results. These results validate our numerical implementation as well as reiterate the mesh objectivity of gradient damage theories in contrast to localized damage theories that yield mesh-sensitive results. In the subsequent examples we select a suitably resolved mesh in our calculations.
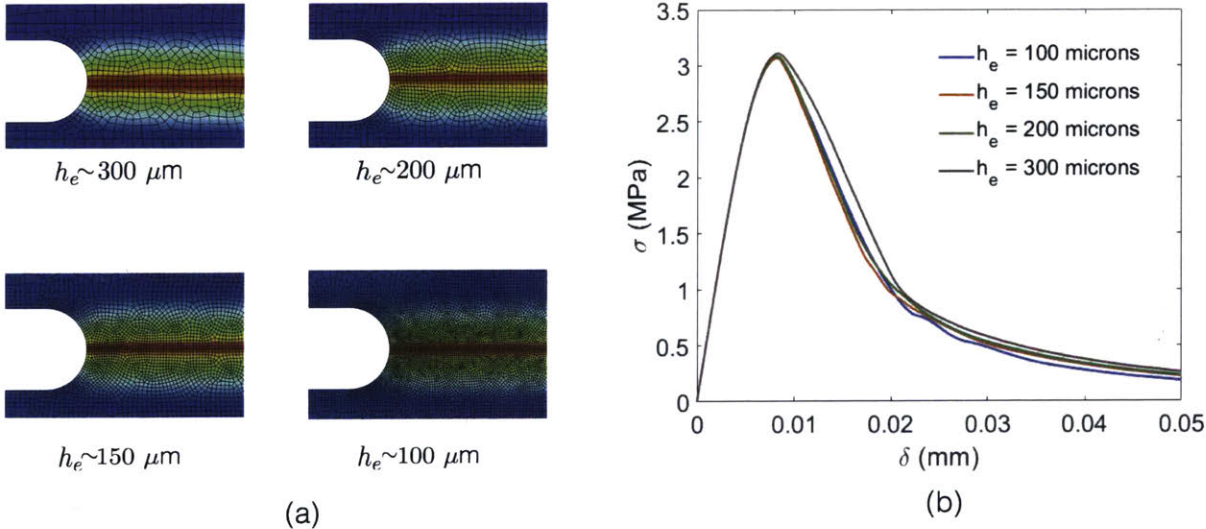

Figure 3-5: (a) The damage contours (b) $\sigma - \delta$ response for the different direct tension test cases with varying mesh resolution

3.2 Three-point un-notched and notched bend tests

As noted by Hoover et al. (2013),

"Although hundreds of concrete fracture tests exist, their evaluation is ambiguous because they have limited ranges of specimen size, initial notch depth and post-peak response, and refer to different concretes, different batches of concrete, different ages, different environmental conditions, different loading rates and test procedures, and different specimen types."

So they conducted an extensive experimental investigation of their own. Amongst the various results presented in their paper was data from three-point bend tests on un-notched and notched beams with crack depths ranging from 0% to 30% of the beam depth, and a broad range of specimen sizes — *all made from one batch of concrete.* The specimens were tested at essentially the same age under carefully-controlled conditions. The geometry of their beams is shown schematically in Fig. 3-6(a), while Fig. 3-6(b) shows a photograph of the different sizes of the beams. With D denoting the depth of the beam, they made beams of length $L = 2.4D$, and tested four families of beams of dimensions $D \times L$ of

$$40 \times 96, \quad 93 \times 223.2, \quad 215 \times 516, \quad \text{and} \quad 500 \times 1200 \, \text{mm},$$

which contained notches of 1.5 mm width and five different relative depths

$$\alpha = 0, \quad 0.025, \quad 0.075, \quad 0.15, \quad \text{and} \quad 0.3,$$

with $\alpha = 0$ representing an un-notched beam. The thickness of all beams was 40 mm. The span between the top two rollers was $S = 2.176H$, and the crack mouth opening displacement (CMOD) δ was measured by either an extensometer bridging the notch mouth, or by an LVDT spanning a sufficient distance on the tensile face of the beam for the un-notched beams. The P-δ response from their three-point bend experiments is given in Fig. 8 of their paper (Hoover et al., 2013).

We have conducted numerical simulations corresponding to a number (not all) of different cases investigated experimentally by Hoover et al. (2013).[2] Fig. 3-6(c) shows a representative snapshot of the deformed geometry with a plot of the damage contours from one of the simulations for a beam of depth $D = 93$ mm and $\alpha = 0.3$. The numerically-calculated P-δ responses are shown in Fig. 3-7(a) through (f) as (solid blue lines), and compared against the corresponding experimentally-reported

---

[2]We used the symmetry of the three-point bend geometry and used a finite element mesh of only one-half of the specimen.

results (solid gray lines).

(a)

(b)

(c)
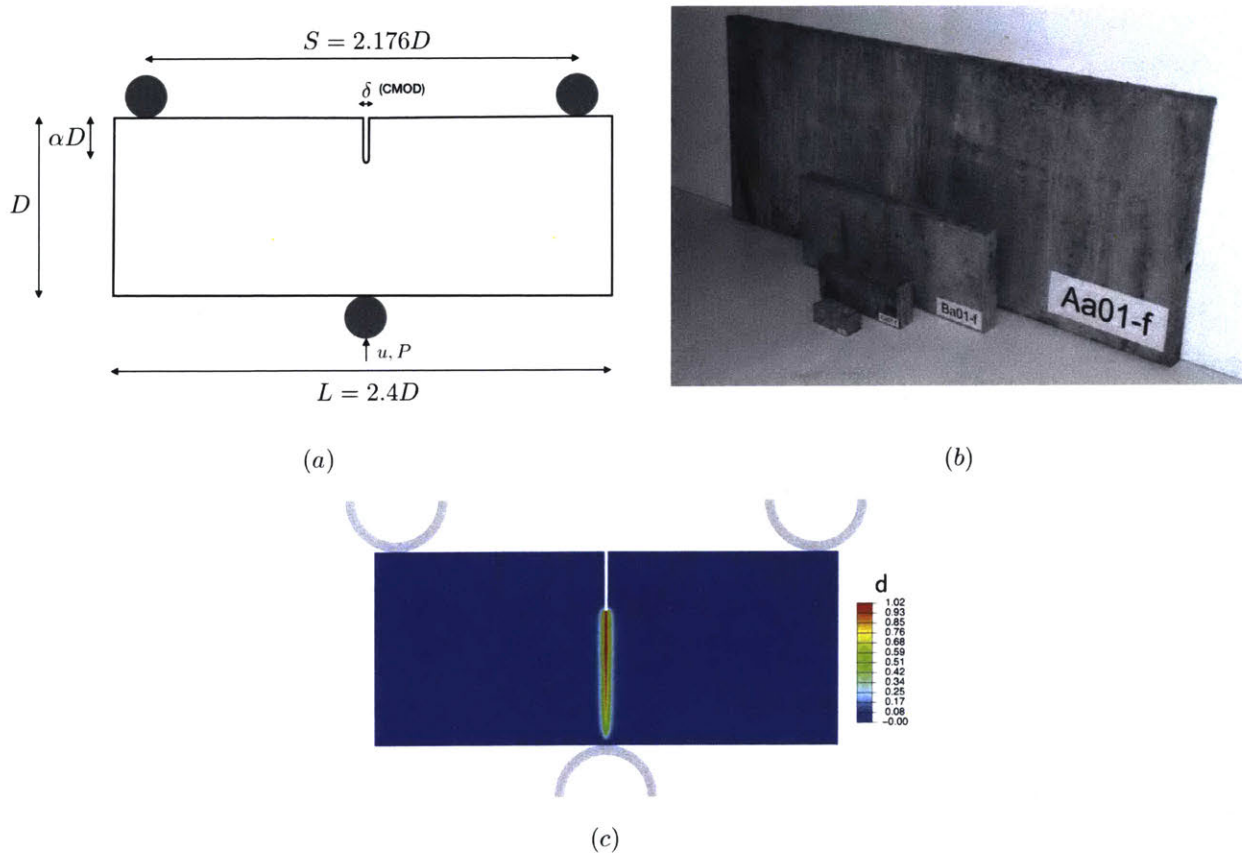
Figure 3-6: (a) Schematic of the geometry of the three-point bend specimens. (b) Photograph of the different sizes of beams with notch depth of $\alpha = 0.3$; from Hoover et al. (2013). (c) A typical plot of the damage contours from one of the simulations for $D = 93$mm and $\alpha = 0.3$

Fig. 3-7(a) through (c) show results corresponding to tests performed on specimens of the same depth, $D = 93$ mm, but with the notch depth varied from $\alpha = 0$, to the beam with the deepest notch, $\alpha = 0.3$. Note the different scale for the vertical load axis in these figures. As can be seen, with increasing notch depth the value of the peak load falls by more than half from ≈ 8 kN in (a) to ≈ 3.5 kN in (c).

Fig. 3-7(d) through (f) show results corresponding to tests performed on specimens of the same notch depth, $\alpha = 0.3$, but with the specimen depth varied from the smallest, $D = 40$ mm to the largest, $D = 500$ mm. Again note the different scale for the vertical load axis in these figures. With increasing specimen depth the value of the peak load increases by a factor of ≈ 6, from a low value

of $\approx 1.75\,\text{kN}$ in (d) to ahigh value of $\approx 11\,\text{kN}$ in (f).
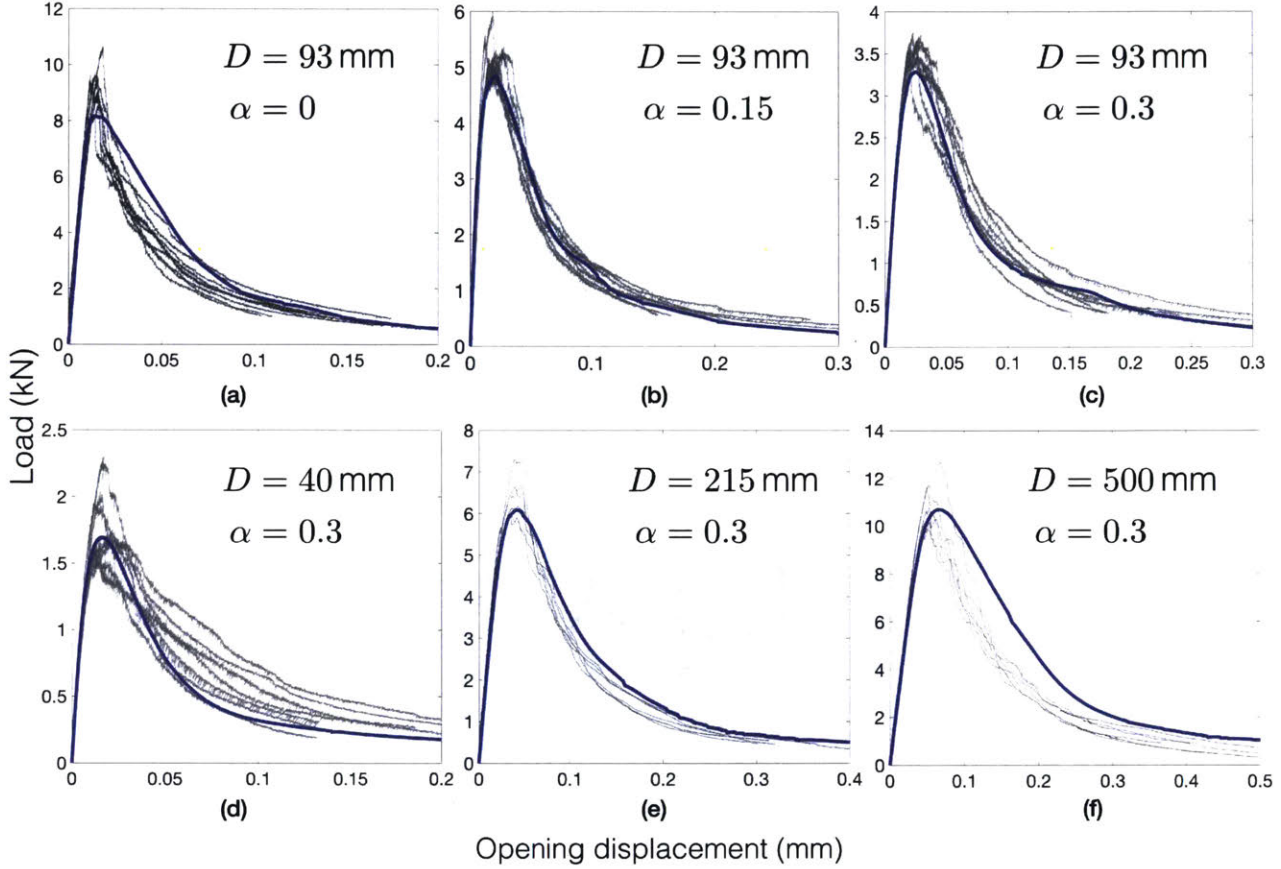
Figure 3-7: Comparison of the the numerically-calculated $P\text{-}\delta$ results (blue lines) against the experimentally-measured response (gray lines).

Table 3.2: Material parameters for three-point bend simulations

E, GPa	ν	S^c, MPa	$\varkappa$	ϵ^c_{crit}	ψ_*, kJ/m^3	ℓ, mm	ζ, kPa-s
41	0.17	4.5	0.7	4.4×10^{-4}	3.8	2	40

The material parameters used in our three-point bend calculations are given in Table 3.2. We note that:

- We have used the values of E and ν reported by Hoover et al. (2013) for their concrete, and we have used the $P\text{-}\delta$ data from only two cases, Fig. 3-7(b) and (e), to calibrate the remaining

material parameters in our model.

- The remaining cases shown in Fig. 3-7 are predictions based on this set of calibrated material parameters.

As can be seen from Fig. 3-7, the numerically calculated response from our model matches the experimental results quite well for both cases used for material parameter calibration. More importantly, the predictions for the other cases are also in reasonable agreement with the experiments. The satisfactory blind predictions of the P-δ response across this wide range of sizes and for both unnotched as well as the notched specimen, convincingly shows the ability of our model to satisfactorily simulate the deformation and fracture response of concrete — at least in the three-point bend configuration tested by Hoover et al. (2013).

3.3   Mixed-mode notched bend tests

We turn next to an application of the theory to calculate the macroscopic load versus crack mouth opening displacement curves as well as the crack trajectories under mixed-mode conditions, as reported by Galvez et al. (1998) in their notched bend tests on concrete. The geometry of their specimens and the loading conditions are shown schematically in Fig. 3-8. They conducted experiments on beams of three different depths: 75 mm, 150 mm and 300 mm. Here we focus on their medium-sized beams of depth 150 mm, which were 675 mm long and 50 mm thick. The beams were notched at their midspan, with a notch width of 2mm and notch depth of 75 mm. The asymmetric three-point bend geometry shown in Fig. 3-8(a) corresponds to what they call their Type 1 experiments, and the asymmetric four-point bend geometry shown in Fig. 3-8(b) corresponds to their Type 2 experiments. The crack mouth opening displacement (CMOD) δ was measured by an extensometer bridging the mouth of the notches. Because of the asymmetric bending, the crack no longer propagates straight across the narrowest cross section. Galvez et al. (1998) reported results for the crack trajectories for their Type 1 and Type 2 experiments in Fig. 3(b) of their paper, and the P-δ response for their Type 1 experiments in their Fig. 5(a), and the P-δ response for their Type 2 experiments in their Fig. 8(a).
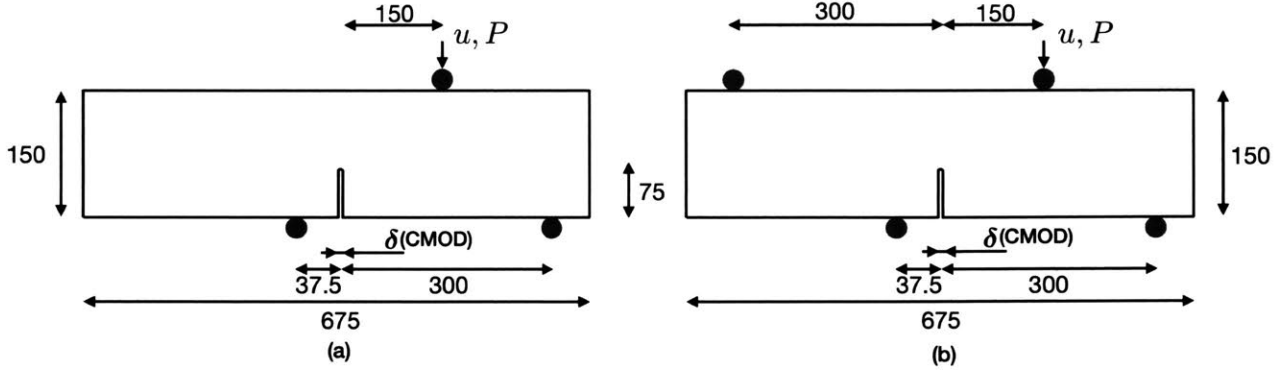
Figure 3-8: Schematic of the specimen geometry and loading conditions for the mixed-mode notched bend experiments of Galvez et al. (1998): (a) Type 1, three-point bending. (b) Type 2, four-point bending. All dimensions in mm.

Table 3.3: Material parameters for mixed-mode notched bend simulations

E, GPa	ν	S^c, MPa	$\varkappa$	$\epsilon^c_{\mathrm{crit}}$	ψ_*, kJ/m^3	ℓ, mm	ζ, kPa-s
38	0.2	3.1	0.7	2.5×10^{-4}	2.1	3	40

Using the material parameters listed in Table 3.3, in Fig. 3-9(a) and (b) we show our numerically-predicted contours of the damage field and the crack trajectory ($\mathsf{d} = 1$) for the Type 1 and Type 2 experiments. Fig. 3-9(c) and (d) show the corresponding experimentally-observed scatter in the crack trajectories as the shaded gray region in each figure. The numerically-calculated crack trajectories shown in Fig. 3-9(a) and (b) are overlayed as blue lines in Fig. 3-9(c) and (d) to facilitate a comparison of the numerical predictions versus the experimental observations. Our model predictions of the crack trajectories are in good agreement with the experiments for both the three-point and four-point mixed-mode notched bend tests.

As noted by Galvez et al. (1998), the cracks in their experiments were observed to grow in a direction normal to the direction of the maximum principal stress at the crack-tip, in accordance with the criterion based on linear elastic fracture mechanics proposed by Erdogan and Sih (1963).[3] The crack trajectories are well-predicted by our non-linear theory for fracture of quasi-brittle materials because the inelastic craze flow direction (which precedes damage initiation and growth to final

---

[3] Also see Carpinteri et al. (1993), who found that their cohesive crack model which dissipates energy only on Mode I, was able to reproduce experimental results from a single-edge notched specimens of concrete subjected to four-point shear to a very good approximation. They concluded that fracture in concrete predominantly propagates in Mode I.

fracture) has been presumed to occur in the direction of the maximum principal tensile stress. *Therefore, the orientation of the damage zones and the crack trajectories are built-in features of our theory.*
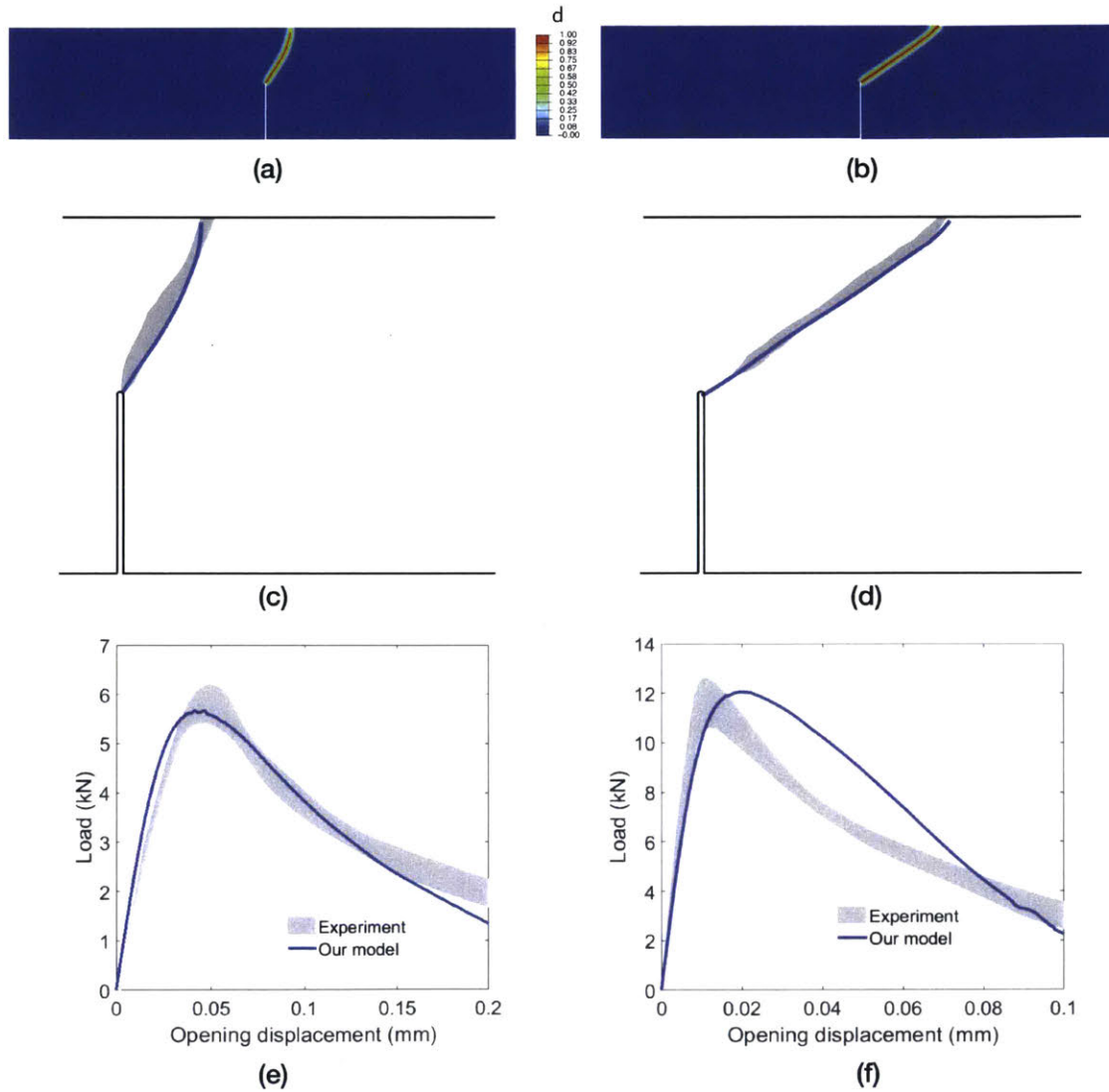
Figure 3-9: (a) and (b) show the numerically-predicted contours of the damage field and the crack trajectory (d = 1) for the Type 1 three-point bend, and the Type 2 four-point bend experiments. (c) and (d) show the corresponding experimentally-observed scatter in the crack trajectories as the shaded-gray region. The numerically-calculated crack trajectories shown in (a) and (b) are overlayed as blue lines for ease of comparison of the numerical predictions and the experimental observations. (e) and (f) compare the numerically-predicted load versus CMOD curves with the corresponding experimentally-measured responses which are shown as gray-shaded scatter ranges. Experimental curves from Galvez et al. (1998).

The numerically-predicted P-δ responses for the two mixed-mode notched bend tests are shown as blue lines in Figs. 3-9 (e) and (f), and compared with the corresponding experimentally-measured responses which are shown as gray-shaded bands. The agreement of the numerical prediction for the Type 1 experiment in Fig. 3-9(e) is good, but that for the Type 2 experiment in Fig. 3-9(f) is not as good. It is important to note that while we used the same set of material parameters listed in Table 3.3 for simulating the two different types of tests, the experimental results are from specimens made from *two different batches* of concrete. Given the variablity in the mechanical properties of concrete from different batches — a variability which was recognized by Galvez et al. in their paper — we consider the prediction shown for the Type 2 four-point notch-bend experiment in Fig. 3-9(f) to be acceptably close to that in the experiments.

3.4 L-shaped panel

In recent years the response of an L-shaped panel has become a popular benchmark test for the verification of numerical predictions from models for fracture of concrete. Winkler et al. (2001) have reported results from such experiments. The geometry of their specimen and the boundary conditions are shown schematically in Fig. 3-10(a). The long and the short edges of the L-shaped panel are 500 mm and 250 mm, respectively, and the thickness of the panel is 100 mm. The lower horizontal edge of the vertical leg is fixed, and the bottom edge of the horizontal leg is subjected to a vertical displacement prescribed at a distance of 30 mm from the right edge. Unlike the previous cases studied in this thesis, there is no pre-existing notch in the L-panel specimen. A crack nucleates from the sharp corner, and the trajectory of the cracks (with its scatter) as experimentally-measured by Winkler et al. (2001) is shown as the gray-shaded region in Fig. 3-10(b).

Table 3.4: Material parameters for L-panel simulations

E, GPa	ν	S^c, MPa	$\varkappa$	ϵ^c_{crit}	ψ_*, kJ/m^3	ℓ, mm	ζ, kPa-s
18	0.2	2.5	0.7	4.9×10^{-4}	3.2	4	40

Using the material parameters listed in Table 3.4, in Fig. 3-10(c) we show our numerically-predicted contours of the damage field and the crack trajectory (d = 1). The numerically-calculated crack trajectory shown in Fig. 3-10(c) is overlayed as the blue line in Fig. 3-10(d) to facilitate a

comparison of the numerical prediction versus the experimental observations. The prediction of the nucleation of the crack and its trajectory from our model is in good agreement with the experimental observation. The corresponding numerically-predicted force versus displacement response is shown by the blue line in Fig. 3-10(e), and compared with the corresponding experimental range which is shown as the gray-shaded region. Our model reproduces the experimentally-measured load-displacement response with good accuracy.
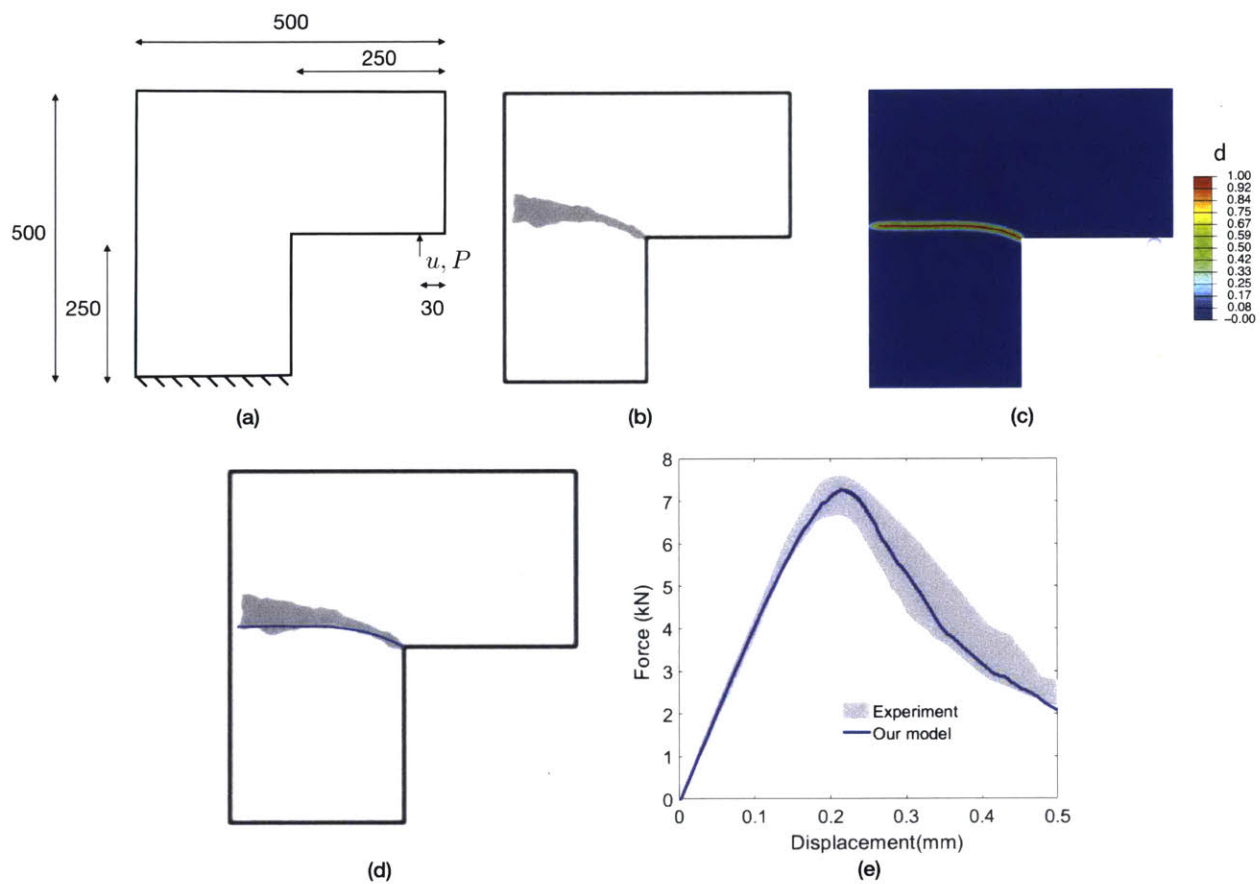
Figure 3-10: (a) Schematic of the specimen geometry and boundary conditions for the L-panel experiments of Winkler et al. (2001); dimensions in mm. (b) Experimentally-observed crack trajectories shown as the gray-shaded region. (c) Numerically-predicted contours of the damage field and the crack trajectory (d = 1) (d) The numerically-calculated crack trajectories shown in (c) is overlayed as the blue line for ease of comparison of the numerical prediction and the experimental observation. (e) Numerically-predicted load versus displacement curve blue line, compared with the corresponding experimentally range which is shown as the gray-shaded region.

Chapter 4

Conclusion

We have formulated a new gradient-damage theory for fracture of quasi-brittle materials and specialized it to model the response of concrete. We have numerically implemented our theory as a user-element subroutine (UEL) in Abaqus (2017), and used this numerical capability to simulate the response of concrete in several important experimental geometries:

(i) Direct tension experiments on symmetrically double-notched specimens of Hordijk (1991).

(ii) Several symmetrically loaded un-notched and notched three-point bend tests of a large range of specimen sizes of Hoover et al. (2013).

(iii) Mixed-mode three-point and four-point notch-bend specimens of Galvez et al. (1998).

(iv) L-shaped panel tests without a notch of Winkler et al. (2001).

The results from these numerical calculations show the ability of our theory and simulation capability to satisfactorily reproduce the macroscopic load-deflection characteristics as well as crack-propagation trajectories during the failure of concrete.

The good correspondence of the results from our numerical simulations and available experimental data indicates that our theory and numerical simulation capability should be of practical utility in the design and analysis of structures made from concrete under largely tensile dominated stress states, the ones that usually control structural failure.

Some directions for future work are: (i) to extend the numerical simulation capability to model fracture of concrete in three-dimensions; (ii) to account for inertial effects; and (iii) to extend the theory to model fracture of high-performance concrete with dispersed polymeric fibers (cf., e.g., Li, 2003). Also, because of the great variability of the microstructure of concrete, the results of macroscopic force-deflection curves and crack trajectories show substantial variability. Whenever data is scattered a probabilistic treatment is required — we also leave such an effort to future work.

Bibliography

Abaqus. Abaqus standard, v 6.17. Simulia-Dassault Systèmes, 2017.

M. Ambati, T. Gerasimov, and L. De Lorenzis. A review on phase-field models of brittle fracture and a new fast hybrid formulation. *Computational Mechanics*, 55:383–405, 2015.

L Anand. On Hencky's approximate strain-energy function for moderate deformations. *ASME Journal of Applied Mechanics*, 46:78–82, 1979.

A. S. Argon and J. G. Hannoosh. Initiation of crazes in polystyrene. *The Philosophical Magazine: A Journal of Theoretical Experimental and Applied Physics*, 36(5):1195–1216, 1977.

Zdenek P. Bazant and B. H. Oh. Crack band theory for fracture of concrete. *Matériaux et Construction*, 16(3):155–177, May 1983.

Zdenek P. Bazant and J. Planas. *Fracture and Size Effect in Concrete and Other Quasibrittle Materials*. CRC Press, 1998.

Z.P. Bazant and J-L. Le. *Probabilistic mechanics of quasibrittle structures: strength, lifetime, and size effect*. Cambridge Univeristy Presss, 2017.

M.J. Borden, C.V. Verhoosel, M.A. Scott, T.J.R. Hughes, and C.M. Landis. A phase-field description of dynamic brittle fracture. *Computer Methods in Applied Mechanics and Mechanical Engineering*, 217-220:77–95, 2012.

Blaise Bourdin, Gilles A Francfort, and Jean-Jacques Marigo. Numerical experiments in revisited brittle fracture. *Journal of the Mechanics and Physics of Solids*, 48(4):797–826, 2000.

Blaise Bourdin, Gilles A. Francfort, and Jean-Jacques Marigo. The variational approach to fracture. *Journal of Elasticity*, 91(1):5–148, 2008.

A. Carpinteri, S. Valente, G. Ferrara, and G. Melchiorri. Is mode II fracture energy a real material property? *Computers and Structures*, 48:397–413, 1993.

Shawn A. Chester, Claudio V. Di Leo, and Lallit Anand. A finite element implementation of a coupled diffusion-deformation theory for elastomeric gels. *International Journal of Solids and Structures*, 52:1 – 18, 2015.

M. Elices, G.V. Guinea, J. Gomez, and J. Planas. The cohesive zone model: advantages, limitations and challenges. *Engineering Fracture Mechanics*, 69(2):137 – 163, 2002.

F. Erdogan and G.C. Sih. On the crack extension in plates under plane loading and transverse shear. *Journal of Basic Engineering*, 85:519–527, 1963.

Gilles A Francfort and J-J Marigo. Revisiting brittle fracture as an energy minimization problem. *Journal of the Mechanics and Physics of Solids*, 46(8):1319–1342, 1998.

M. Fremond and B. Nedjar. Damage, gradient of damage, and principle of virtual power. *International Journal of Solids and Structures*, 33:1083–1103, 1996.

J.C. Galvez, M. Elices, G.V. Guinea, and J. Planas. Mixed mode fracture of concrete under proportional and nonproportional loading. *International Journal of Fracture*, 94(3):267–284, 1998.

BP Gearing and L Anand. On modeling the deformation and fracture response of glassy polymers due to shear-yielding and crazing. *International Journal of Solids and Structures*, 41(11-12): 3125–3150, 2004.

P. Germain. The method of virtual power in continuum mechanics. Part 2: microstructure. *SIAM Journal of Applied Mathematics*, 25:556–575, 1973.

M.E. Gurtin. Generalized Ginzburg-Landau and Cahn-Hilliard equations based on a microforce balance. *Physica D*, 92:178–192, 1996.

M.E. Gurtin. A gradient theory of single-crystal viscoplasticity that accounts for geometrically necessary dislocations. *Journal of the Mechanics and Physics of Solids*, 50:5–32, 2002.

Morton E Gurtin, Eliot Fried, and Lallit Anand. *The mechanics and thermodynamics of continua.* Cambridge University Press, 2010.

A. Hillerborg, M. Modeer, and P.E. Petersson. Analysis of crack formation and crack growth in concrete by means of fracture mechanics. *Cement and Concrete Research*, 6:773–782, 1976.

Christian Hoover and Zdenek P. Bazant. Cohesive crack, size effect, crack band and work-of-fracture models compared to comprehensive concrete fracture tests. *International Journal of Fracture*, 187 (1):133–143, 2014.

Christian G. Hoover, Zdenek P. Bazant, Jan Vorel, Roman Wendner, and Mija H. Hubler. Comprehensive concrete fracture tests: Description and results. *Engineering Fracture Mechanics*, 114:92 – 103, 2013.

D.A. Hordijk. Local approach to fatigue of concrete. *Thesis-TU Delft*, 1991.

C. Ishiyama, T. Asai, M. Kobayashi, M. Shimojo, and Y. Higo. Fatigue crack propagation mechanisms in poly(methyl methacrylate) by in situ observation with a scanning laser microscope. *Journal of Polymer Science Part B: Polymer Physics*, 39(24):3103–3113, 2001.

V. Li. On engineered cementitious composites (ECC). *Journal of advanced concrete technology*, 1: 215230, 2003.

Eric Lorentz. A nonlocal damage model for plain concrete consistent with cohesive fracture. *International Journal of Fracture*, 207(2):123–159, 2017.

C. Miehe, M. Hofacker, and F. Welschinger. A phase field model for rate-independent crack propagation: robust algorithmic implementation based on operator splits. *Computer Methods in Applied Mechanics and Engineering*, 199:2765–2778, 2010a.

C. Miehe, F. Welschinger, and M. Hofacker. Thermodynamically consistent phase-field models of fracture: variational principles and multi-field FE implementations. *International Journal of Numerical Methods in Engineering*, 83:1273–1311, 2010b.

C. Miehe, L.M. Schänzel, and H. Ulmer. Phase field modeling of fracture in multiphysics problems. Part I. Balance of crack surface and failure criteria for brittle crack propagation in thermo-elastic solids. *Computer Methods in Applied Mechanics and Engineering*, 294:449–485, 2015.

Christian Miehe, Fadi Aldakheel, and Arun Raina. Phase field modeling of ductile fracture at finite strains: A variational gradient-extended plasticity-damage theory. *International Journal of Plasticity*, 84:1–32, 2016.

R.H.J. Peerlings, R. De Borst, W.A.M. Brekelmans, and J.H.P. De Vree. Gradient enehanced damage models for quasi-brittle fracture. *International Journal for Numerical Methods in Engineering*, 39(19):3391–3403, 1996.

R.H.J. Peerlings, R. de Borst, W.A.M. Brekelmans, and M.G.D. Geers. Gradient-enhanced damage modelling of concrete fracture. *Mechanics of Cohesive-frictional Materials*, 3(4):323–342, 1998.

P.E. Petersen. Crack growth and development of fracture zones in plain concrete and similar materials. Technical Report Report TVBM-1006, Lund Institute of Technology, 1981.

K.H. Pham, K. Ravi-Chandar, and C.M. Landis. Experimental validation of a phase-field model for fracture. *International Journal of Fracture*, 205:83–101, 2017.

Gilles Pijaudier-Cabot and Zdenek P. Bazant. Nonlocal damage theory. *Journal of Engineering Mechanics*, 113(10):1512–1533, 1987.

E. Schlangen and J.G.M. van Mier. Experimental and numerical analysis of micromechanisms of fracture of cement-based composites. *Cement and Concrete Composites*, 14(2):105 – 118, 1992. Special Issue on Micromechanics of Failure in Cementitious Composites.

Pavel Trtik, P Stahli, Eric Landis, Marco Stampanoni, and J.G.M. Van Mier. Microtensile testing and 3D imaging of hydrated Portland cement. *Proceedings of the 6th International Conference on Fracture Mechanics of Concrete and Concrete Structures*, 3:1277–1282, 01 2007.

J.G.M. Van Mier. Mode I fracture of concrete: discontinuous crack growth and crack interface grain bridging. *Cement and Concrete Research*, 21:1–15, 1991.

S. Wang and V.C. Li. Tailoring of pre-existing flaws in ECC matrix for saturated strain hardening. In *Fracture Mechanics of Concrete Structures*, pages 1005–112, 2004.

Gustavo Weber and Lallit Anand. Finite deformation constitutive equations and a time integration procedure for isotropic, hyperelastic-viscoplastic solids. *Computer Methods in Applied Mechanics and Engineering*, (79):173–202, 1990.

B Winkler, G Hofstetter, and G Niederwanger. Experimental verification of a constitutive model for concrete cracking. *Proceedings of the Institution of Mechanical Engineers, Part L: Journal of Materials: Design and Applications*, 215(2):75–86, 2001.

Jian-Ying Wu. A unified phase-field theory for the mechanics of damage and quasi-brittle failure. *Journal of the Mechanics and Physics of Solids*, 103:72 – 99, 2017.

Jian-Ying Wu, Vinh Phu Nguyen, Chi Thanh Nguyen, Danas Sutula, Stephane Bordas, and Sina Sinaie. Phase field modeling of fracture. *Advances in Applied Mechanics: Multi-scale Theory and Computation*, 52:1–115, 2018.

Numerical implementation details

A.1 Implementation in ABAQUS/Standard

We have numerically implemented our theory as a user-element (UEL) subroutine in the implicit finite element program Abaqus/Standard (Abaqus, 2017) by following the implementation procedures detailed in Chester et al. (2015). Our numerical implementation is for a plane-strain scenario and uses a linear 4-noded plane-strain element. At the constitutive level the time integration procedure in our numerical implementation is by an implicit backward-Euler scheme. At the global level the deformation problem and the damage problem are solved using a staggered scheme.

A.2 Residuals and Tangents

Displacement governing equation

The displacement solution variables are governed by the partial differential equation for the balance of momentum (see (2.124)), the strong form of which, in the *current* configuration, along with

appropriate boundary conditions is given by

$$\left.\begin{array}{rcll} \mathrm{div}\mathbf{T} &=& \mathbf{0} & \text{on} \quad \mathrm{B}_t, \\[2mm] \mathbf{u} &=& \breve{\mathbf{u}} & \text{on} \quad \mathcal{S}_1, \\[2mm] \mathbf{Tn} &=& \breve{\mathbf{t}} & \text{on} \quad \mathcal{S}_2, \end{array}\right\} \tag{A.1}$$

where B_t denotes the body in the current deformed configuration, on the deformed surface $\mathcal{S}_1$ we prescribe displacements, and on the deformed surface $\mathcal{S}_2$ we prescribe surface tractions. To find the weak form of (A.1) we multiply by a test function $\mathbf{w}$ and integrate over the body

$$0 = \int_{\mathrm{B}_t} (\mathbf{w} \cdot \mathrm{div}\mathbf{T}) \, dV \tag{A.2}$$

which integrating by parts yields

$$0 = \int_{\mathrm{B}_t} (-\mathrm{grad}\,\mathbf{w} : \mathbf{T}) \, dV + \int_{\partial \mathrm{B}_t} (\mathbf{w} \cdot \mathbf{Tn}) \, dA, \tag{A.3}$$

and using $(A.1)_3$ we have

$$0 = \int_{\mathrm{B}_t} (-\mathrm{grad}\,\mathbf{w} : \mathbf{T}) \, dV + \int_{\mathcal{S}_1} (\mathbf{w} \cdot \breve{\mathbf{t}}) \, dA. \tag{A.4}$$

The body is approximated using finite elements $\mathrm{B}_t = \sum \mathrm{B}_t^e$ and the trial solution for the displacement vector is interpolated inside each element by

$$\mathbf{u} = \sum_A N^A \mathbf{u}^A \tag{A.5}$$

with the index $A = 1, 2, \ldots$ denoting the nodes of the element, $\mathbf{u}^A$ denoting the nodal displacement vector, and N^A the shape functions. We employ a standard Galerkin approach, in that the weighting field is interpolated by the same shape functions, such that

$$\mathbf{w} = \sum_A N^A \mathbf{w}^A. \tag{A.6}$$

This yields the element-level relation

$$0 = \int_{B_t^e} (-\mathbf{w}^A \cdot (\mathbf{T} \text{grad} \, N^A)) \, dV + \int_{\mathcal{S}_1^e} (N^A \mathbf{w}^A \cdot \check{\mathbf{t}}) \, dA \qquad (A.7)$$

which must hold for all $\mathbf{w}^A$. Therefore, we define the element level displacement residual

$$\mathbf{R}_{\mathbf{u}}^A = \int_{B_t^e} (-\mathbf{T} \text{grad} \, N^A) \, dV + \int_{\mathcal{S}_1^e} (N^A \check{\mathbf{t}}) \, dA, \qquad (A.8)$$

which in index notation is

$$R_{u_i}^A = \int_{B_t^e} \left(-T_{ij} \frac{\partial N^A}{\partial x_j} \right) dV + \int_{\mathcal{S}_1^e} (N^A \check{t}_i) \, dA. \qquad (A.9)$$

The element stiffness/tangent is given by

$$\mathbf{K}_{\mathbf{uu}}^{AB} = -\frac{\partial \mathbf{R}_{\mathbf{u}}^A}{\partial \mathbf{u}^B}, \quad \text{or in index notation} \quad K_{u_i u_k}^{AB} = -\frac{\partial R_{u_i}}{\partial u_k^B}. \qquad (A.10)$$

Using the residual defined above we have

$$K_{u_i u_k}^{AB} = \int_{B_t^e} \frac{\partial N^A}{\partial x_j} \frac{\partial T_{ij}}{\partial u_k^B} \, dV - \int_{\mathcal{S}_1^e} N^A N^B \frac{\partial \check{t}}{\partial u_k} \, dA. \qquad (A.11)$$

Furthermore,

$$\frac{\partial T_{ij}}{\partial u_k^B} = \frac{\partial T_{ij}}{\partial F_{mn}} \frac{\partial F_{mn}}{\partial u_k^B}, \qquad (A.12)$$

and since

$$F_{mn} = \delta_{mn} + \frac{\partial N^A}{\partial x_n} u_m^A, \quad \text{and} \quad \frac{\partial F_{mn}}{\partial u_k^B} = \frac{\partial N^B}{\partial x_n} \delta_{mk}, \qquad (A.13)$$

we arrive at

$$K_{u_i u_k}^{AB} = \int_{B_t^e} \frac{\partial N^A}{\partial x_j} \frac{\partial T_{ij}}{\partial F_{kn}} \frac{\partial N^B}{\partial x_n} \, dV - \int_{\mathcal{S}_1^e} N^A N^B \frac{\partial \check{t}}{\partial u_k} \, dA. \qquad (A.14)$$

In computing the term $\partial T_{ij}/\partial F_{kn}$ in the stiffness matrix, we utilize a numerical perturbation method as follows :

- We perturb one out of the nine components of the deformation gradient by a small but finite value : $\approx 10^{-6}$

81

- We evaluate the Cauchy stress tensor (with damage) based on our model as outlined in the time integration procedure in section A.3

- We repeat the perturbation for each component of the deformation gradient sequentially to obtain a numerical approximation to the 4th order tensor $\partial T_{ij}/\partial F_{kn}$.

Damage governing equation

The damage variables are governed by the partial differential equation for the evolution of the damage variable (see (2.125)). The strong form complemented by the boundary condition is given as:

$$\left.\begin{aligned} \zeta\,\dot{\mathsf{d}} &= 2(1-\mathsf{d})\,\mathcal{H} - 2\psi_*(\mathsf{d} - \ell^2\,\Delta\mathsf{d}), \\ (\nabla\mathsf{d})\cdot\mathbf{n}_{\mathrm{R}} &= 0 \quad \text{on } \mathcal{S} \end{aligned}\right\} \tag{A.15}$$

To find the weak form of (A.15) we multiply by a test function w and integrate over the body as,

$$0 = \int_{\mathrm{B}} w(\zeta\,\dot{\mathsf{d}} - 2(1-\mathsf{d})\,\mathcal{H} + 2\psi_*(\mathsf{d} - \ell^2\,\Delta\mathsf{d}))\,dV_{\mathrm{R}} \tag{A.16}$$

As earlier, integration by parts gives

$$0 = \int_{\mathrm{B}} w\left[\zeta\,\dot{\mathsf{d}} - 2(1-\mathsf{d})\,\mathcal{H} + 2\psi_*(\mathsf{d})\right]dV_{\mathrm{R}} + \int_{\mathrm{B}} 2\psi_*\ell^2(\nabla w \cdot \nabla\mathsf{d})\,dV_{\mathrm{R}} - \int_{\partial\mathrm{B}} 2\psi_*\ell^2 w(\nabla\mathsf{d}\cdot\mathbf{n}_{\mathrm{R}})\,dA_{\mathrm{R}} \tag{A.17}$$

Use of (A.15) in the last term on the right gives

$$0 = \int_{\mathrm{B}} w\left[\zeta\,\dot{\mathsf{d}} - 2(1-\mathsf{d})\,\mathcal{H} + 2\psi_*(\mathsf{d})\right]dV_{\mathrm{R}} + \int_{\mathrm{B}} 2\psi_*\ell^2(\nabla w \cdot \nabla\mathsf{d})\,dV_{\mathrm{R}} \tag{A.18}$$

The body is approximated using finite elements $\mathrm{B} = \sum \mathrm{B}^e$ and the trial solution for the damage variable is interpolated inside each element by

$$\mathsf{d} = \sum_{A} N^A \mathsf{d}^A \tag{A.19}$$

with the index $A = 1, 2, \ldots$ denoting the nodes of the element, d^A denoting the nodal damage field, and N^A the shape functions. We again employ a standard Galerkin approach, such that

$$w = \sum_A N^A w^A. \tag{A.20}$$

Subsequently, we have element-level relations for our finite-element framework as

$$0 = \int_{\mathrm{B}^e} w^A N^A \left[\zeta \, \dot{\mathsf{d}} - 2(1 - \mathsf{d}) \, \mathcal{H} + 2\psi_*(\mathsf{d}) \right] dV_{\mathrm{R}} + \int_{\mathrm{B}^e} 2\psi_* \ell^2 (\nabla N^A \cdot \nabla \mathsf{d}) w^A \, dV_{\mathrm{R}} \tag{A.21}$$

which hold for every test function w^A. Therefore, we define the element level residual,

$$R_{\mathsf{d}}^A = \int_{\mathrm{B}^e} N^A \left[\zeta \, \dot{\mathsf{d}} - 2(1 - \mathsf{d}) \, \mathcal{H} + 2\psi_*(\mathsf{d}) \right] dV_{\mathrm{R}} + \int_{\mathrm{B}^e} 2\psi_* \ell^2 (\nabla N^A \cdot \nabla \mathsf{d}) \, dV_{\mathrm{R}}. \tag{A.22}$$

The element stiffness is given by

$$K_{\mathsf{dd}}^{AB} = -\frac{\partial R_{\mathsf{d}}^A}{\partial \mathsf{d}^B} \tag{A.23}$$

Using the residual defined above we have

$$K_{\mathsf{dd}}^{AB} = \int_{\mathrm{B}^e} N^A \left[\zeta \, N^B \frac{1}{\Delta t} - 2(-N^B) \, \mathcal{H} + 2\psi_*(N^B) \right] dV_{\mathrm{R}} + \int_{\mathrm{B}^e} 2\psi_* \ell^2 (\nabla N^A \cdot \nabla N^B) \, dV_{\mathrm{R}}. \tag{A.24}$$

We use a staggered formulation for the coupled damage-deformation system in our ABAQUS/Standard User Element subroutine(UEL) implementation. Hence the mixed tangent terms $\mathbf{K_{du}}$ and $\mathbf{K_{ud}}$ are not of importance and we do not evaluate them here.

A.3   Time Integration Procedure

The summary of the time integration procedure implemented in the UEL subroutine for our model is as follows:

Step 0. Given $\{\mathbf{F}_n^c, \, \epsilon^c{}_n, \, \mathbf{e}_n^{cr}\}$[1] at time t_n, and $\{\mathbf{F}_{n+1}, \mathsf{d}_{n+1}\}$ at time $t_{n+1} = t_n + \Delta t$, we wish to evaluate $\{\mathbf{T}_{n+1}, \, \mathbf{F}_{n+1}^c, \, \epsilon^c{}_{n+1}, \, \mathbf{e}_{n+1}^{cr}\}$ at time t_{n+1}.

---

[1]$\mathbf{e}^{cr}$ is the direction for craze extension which coincides with the first principal direction of the Mandel stress $\mathbf{e}_1$.

Step 1. Calculate the trial elastic deformation gradient as

$$\mathbf{F}^e_{\text{trial}} = \mathbf{F}_{n+1} \mathbf{F}^{c-1}_n.$$

(A.25)

Step 2. Perform the polar decomposition

$$\mathbf{F}^e_{\text{trial}} = \mathbf{R}^e_{\text{trial}} \, \mathbf{U}^e_{\text{trial}}.$$

(A.26)

Perform the spectral decomposition of $\mathbf{U}^e_{\text{trial}}$ and calculate trial logarithmic elastic strain as

$$\mathbf{E}^e_{\text{trial}} = \ln \mathbf{U}^e_{\text{trial}} = \sum_{i=1}^e \ln \lambda^e_{i\,\text{trial}} \, \mathbf{r}^e_{i\,\text{trial}} \otimes \mathbf{r}^e_{i\,\text{trial}}.$$

(A.27)

Step 3. Evaluate the trial Mandel stress as

$$\mathbf{M}^e_{\text{trial}} = g(\mathbf{d}) \left[2G\mathbf{E}^e_{\text{trial}} + \lambda \operatorname{tr} \mathbf{E}^e_{\text{trial}} \right],$$

(A.28)

and calculate the maximum principal value (σ_1) of the Mandel stress through spectral decomposition and the hydrostatic stress as

$$\mathbf{M}^e_{\text{trial}} = \sum_{i=1}^e \ln \sigma^e_{i\,\text{trial}} \, \mathbf{e}_{i\,\text{trial}} \otimes \mathbf{e}_{i\,\text{trial}}$$

$$\sigma_h = \frac{1}{3} \operatorname{tr} \mathbf{M}^e$$

(A.29)

Step 4. Check for craze initiation: when $\sigma_h \geq 0$ and $\sigma_1 \geq S_c$ are both satisfied then craze is initiated. Activate a craze flag to indicate craze initiation for use in subsequent time steps.

When crazing is not initiated then the Mandel stress, craze deformation gradient are obtained simply as $\mathbf{M}^e_{n+1} = \mathbf{M}^e_{\text{trial}}$ and $\mathbf{F}^c_{n+1} = \mathbf{F}^c_n$. Go to step 8 directly.

Step 5. When crazing is initiated, set the craze direction tensor as

$$\mathbf{N}^c = \mathbf{e}^{cr}_n \otimes \mathbf{e}^{cr}_n$$

(A.30)

84

Step 6. Evaluate

$$\sigma_{1\,\text{trial}} = \mathbf{M}^e_{\text{trial}} : \mathbf{N}^c \tag{A.31}$$

When $\sigma_{1\,\text{trial}} - g(\mathsf{d})S^c \geq 0$, evaluate craze strain increment as (see section A.4)

$$\Delta\epsilon^c = \frac{\sigma_{1\,\text{trial}} - g(\mathsf{d})S^c}{\mathbb{C}_{1111}} \quad \text{with} \quad \mathbb{C}_{1111} = g(d)E\frac{1-\nu}{(1+\nu)(1-2\nu)} \tag{A.32}$$

Step 7. The craze strain at the end of the step and the craze strain rate are evaluated as

$$\epsilon^c_{n+1} = \epsilon^c_n + \Delta\epsilon^c \qquad \dot{\epsilon}^c = \frac{\Delta\epsilon^c}{\Delta t} \tag{A.33}$$

The craze stretch tensor is calculated as

$$\mathbf{D}^c_{n+1} = \dot{\epsilon}^c \mathbf{N}^c \tag{A.34}$$

The craze deformation gradient is calculated as in (2.12), by means of an exponential map following Weber and Anand (1990),

$$\mathbf{F}^c_{n+1} = \exp(\Delta t \mathbf{D}^c_{n+1})\mathbf{F}^c_n. \tag{A.35}$$

Step 8. The elastic deformation gradient at the end of the step is

$$\mathbf{F}^e_{n+1} = \mathbf{F}_{n+1}\mathbf{F}^{c-1}_{n+1}. \tag{A.36}$$

As earlier, polar decomposition and spectral decomposition leads to the logarithmic elastic strain at end of step

$$\begin{aligned} \mathbf{F}^e_{n+1} &= \mathbf{R}^e_{n+1}\,\mathbf{U}^e_{n+1} \\ \mathbf{E}^e_{n+1} &= \ln\mathbf{U}^e_{n+1} = \sum_{i=1}^{e} \ln\lambda^e_{i\,n+1}\mathbf{r}^e_{i\,n+1} \otimes \mathbf{r}^e_{i\,n+1} \end{aligned} \tag{A.37}$$

Step 9. The Mandel stress at the end of the step is given as

$$\mathbf{M}^e_{n+1} = g(\mathsf{d}) \left[2G\mathbf{E}^e_{n+1} + \lambda \operatorname{tr} \mathbf{E}^e_{n+1} \right].$$ (A.38)

The craze direction tensor at the end of the step is obtained from the spectral decomposition of the Mandel stress as

$$\mathbf{M}^e_{n+1} = \sum_{i=1}^{e} \ln \sigma^e_{i\,n+1} \mathbf{e}_{i\,n+1} \otimes \mathbf{e}_{i\,n+1}$$

$$\mathbf{N}^c_{n+1} = \mathbf{e}^{cr}_{n+1} \otimes \mathbf{e}^{cr}_{n+1} \qquad \text{with} \qquad \mathbf{e}^{cr}_{n+1} = \mathbf{e}_{1\,n+1}$$ (A.39)

Step 10. The Cauchy stress tensor is calculated from Mandel stress as

$$\mathbf{T}_{n+1} = J^{e-1} \mathbf{R}^e_{n+1} \mathbf{M}^e_{n+1} \mathbf{R}^{e\top}_{n+1}$$ (A.40)

This is a brief summary of the time integration procedure which is implemented in the UEL to evaluate the behavior as described by our constitutive model.

A.4 Craze strain increment

The craze strain increment is evaluated based on the following algorithm.

- The trial elastic distortion at the start of the increment is calculated based on the current deformation gradient and the craze deformation from the previous step,

$$\mathbf{F}^e_{\text{trial}} = \mathbf{F}_\tau \mathbf{F}^{c-1}_t.$$ (A.41)

Subsequently, $\mathbf{E}^e_{\text{trial}} = \ln \sqrt{\mathbf{F}^{e\top}_{\text{trial}} \mathbf{F}^e_{\text{trial}}}$ is known.

- The trial Mandel stress and the corresponding principal value is then evaluated as

$$\mathbf{M}^e_{\text{trial}} = g(\mathsf{d}) \left[2G\mathbf{E}^e + \lambda \operatorname{tr} \mathbf{E}^e \mathbf{1} \right] = \sum_{i=1}^{3} \sigma_{i\,\text{trial}} \mathbf{e}_{i\,\text{trial}} \otimes \mathbf{e}_{i\,\text{trial}}.$$ (A.42)

- When $\sigma_{1\,\text{trial}}$ exceeds the damaged craze resistance, i.e $\sigma_{1\text{trial}} > g(\mathsf{d})S^c$, the craze strain

increment is to be evaluated based on the craze flow strength relation $\sigma_1 = g(\mathbf{d})S^c$.

Let us denote by $\Delta\epsilon^c$, the craze strain increment in the present timestep. Then we have

$$\mathbf{D}^c = \frac{\Delta\epsilon}{\Delta t}\mathbf{e}_1 \otimes \mathbf{e}_1 \tag{A.43}$$

Based on an exponential mapping, the craze strain deformation gradient update can then be expressed as

$$\mathbf{F}^c_\tau = \exp\left(\Delta t \mathbf{D}^c\right)\mathbf{F}^c_t = \exp\left(\Delta\epsilon^c \mathbf{e}_1 \otimes \mathbf{e}_1\right)\mathbf{F}^c_t. \tag{A.44}$$

- The elastic deformation gradient at the end of the step can then be given as

$$\mathbf{F}^e_\tau = \mathbf{F}_\tau \mathbf{F}^{c-1}_\tau = \mathbf{F}^e_{\text{trial}} \exp\left(-\Delta\epsilon^c \mathbf{e}_1 \otimes \mathbf{e}_1\right) \tag{A.45}$$

The polar decomposition of the trial and the current deformation gradient leads to

$$\mathbf{R}^e_\tau \mathbf{U}^e_\tau = \mathbf{R}^e_{\text{trial}} \mathbf{U}^e_{\text{trial}} \exp\left(-\Delta\epsilon^c \mathbf{e}_1 \otimes \mathbf{e}_1\right) \tag{A.46}$$

The principal directions of the tensor $\mathbf{e}_1 \otimes \mathbf{e}_1$ are the same as that of the trial Mandel stress tensor $\mathbf{M}^e_{\text{trial}}$, which is also that of $\mathbf{U}^e_{\text{trial}}$. Thereby, the uniqueness of the polar decomposition yields,

$$\mathbf{R}^e_\tau = \mathbf{R}^e_{\text{trial}} \quad \text{and} \quad \mathbf{U}^e_\tau = \mathbf{U}^e_{\text{trial}} \exp\left(-\Delta\epsilon^c \mathbf{e}_1 \otimes \mathbf{e}_1\right). \tag{A.47}$$

- Then based on the definition of the logarithmic strain tensor, we have

$$\mathbf{E}^e_\tau - \mathbf{E}^e_{tr} = -\Delta\epsilon^c \mathbf{e}_1 \otimes \mathbf{e}_1. \tag{A.48}$$

The increment in the principal value of the Mandel stress can be estimated as

$$\Delta\sigma_1 = \mathbf{e}_1 . \left[\mathbb{C}\left(\mathbf{E}^e_\tau - \mathbf{E}^e_{tr}\right)\right]\mathbf{e}_1 \tag{A.49}$$

where $\mathbb{C} = g(d)\mathbb{C}_{\text{elas}}$, with $\mathbb{C}_{\text{elas}}$ the standard fourth order elasticity tensor. Then using the

relation from (A.48)

$$\Delta\sigma_1 = -\Delta\epsilon^c \mathbf{e}_1 . \left[\mathbb{C} \left(\mathbf{e}_1 \otimes \mathbf{e}_1 \right) \right] \mathbf{e}_1 = -\mathbb{C}_{1111}\Delta\epsilon^c \qquad (A.50)$$

where

$$\mathbb{C}_{1111} = g(d)E\frac{1-\nu}{(1+\nu)(1-2\nu)}$$

• Finally, substituting back in the craze flow strength relation, we have

$$\sigma_1 = \sigma_{1\text{trial}} + \Delta\sigma_1 = \sigma_{1\text{trial}} - \mathbb{C}_{1111}\Delta\epsilon^c = g(\mathbf{d})S^c$$

$$\Delta\epsilon^c = \frac{\sigma_{1\text{trial}} - g(\mathbf{d})S^c}{\mathbb{C}_{1111}} \qquad (A.51)$$